Large-Eddy Simulation of the Diurnal Cycle of Deep Equatorial Turbulence

DAILIN WANG, JAMES C. MCWILLIAMS,* AND WILLIAM G. LARGE

National Center for Atmospheric Research,+ Boulder, Colorado

(Manuscript received 25 November 1996, in final form 5 June 1997)

ABSTRACT

The deep diurnal cycle of turbulence at the equator is studied using the technique of large-eddy simulation (LES). Based on a scale-separation hypothesis, the LES model includes the following large-scale flow terms: the equatorial undercurrent (EUC), zonal pressure gradient, upwelling, horizontal divergence, zonal temperature gradient, and mesoscale eddy forcing terms for the zonal momentum and the heat equations. The importance of these terms in obtaining a quasi-equilibrium boundary layer solution is discussed. The model is forced with a constant easterly wind stress and diurnal cooling and heating. It is found that boundary-layer turbulence penetrates as deep as 50 m below the mixed layer during nighttime cooling. The diurnal variation of turbulence dissipation and mixed layer depth are within the range of observations. The gradient Richardson number (Ri) of the mean flow shows a diurnal cycle but the amplitudes decrease with depth. Within the mixed layer and just below the layer, Ri can be lower than the critical value of 0.25 at night. During the day, Ri $>$ 0.25 below the mixed layer. Well below the mixed layer (below about 40 m), Ri is always greater than 0.25 because of the initial vertical profiles of EUC and temperature chosen. However, the flow is still highly nonlinear, or turbulent, as indicated by the order one ratio of fluctuating temperature gradient (root-mean-square) to the mean gradient. The authors find that this deep turbulence cycle from the model is closely related to local shear (or Kelvin–Helmholtz) instability. Distribution of local (pointwise) gradient Richardson number shows a diurnal cycle, which is the cause of the diurnal cycle of turbulence well below the mixed layer as evidenced by high levels of turbulent kinetic energy at local Richardson numbers in the range of [0, 0.25]. Eddy viscosity and diffusivity are computed from the LES solutions and are compared with observationally derived values.

1. Introduction

Observations of turbulence dissipation at the equator (140°W) display a strong diurnal cycle both within and below the mixed layer (Gregg et al. 1985; Moum and Caldwell 1985). The transition from net surface heating during the day to convective surface cooling at night leads to enhanced nighttime turbulence levels that are seen as high dissipation values. However, there is considerable variability in the characteristics of the cycle such as its amplitude and depth dependency. Peters et al. (1994) contrast the results from the first Tropic Heat Experiment (TH1) in November 1984, as detailed in Moum et al. (1989), with the second Tropic Heat Experiment (TH2) in April 1987. They found similar patterns of turbulent variability, but the greater vertical shear, lower stratification, and stronger winds of TH1 were accompanied by a larger average dissipation rate (by a factor of 2 in the upper 30 m), a smaller ratio of night to day dissipation, and a deeper penetration of the dissipation cycle. More recent observations of the Tropical Instability Wave Experiment (TIWE) in November and December of 1991 (Lien et al. 1995) show that turbulence dissipation between the mixed-layer base and the equatorial undercurrent (EUC) can vary diurnally by more than factor of 100 or by less than a factor of 10. Much of this long-term variability is ascribed to the phase of a Kelvin wave that propagated through the observation site.

The physical mechanisms of this deep diurnal cycle of turbulence, or deep-cycle turbulence for short (Lien et al. 1996), are not fully understood. The cycle has been linked to internal wave breaking in the prescence of the equatorial undercurrent shear (Gregg et al. 1985) during nocturnal convective cooling. Peters et al. (1994) showed that enhanced wave activity at night was paralleled by enhanced finescale shear, which was available to induce local flow instability and mixing. Observations (e.g., McPhaden and Peters 1992) show that temperature variance below the mixed layer is enhanced at nighttime, supporting the hypothesis of Gregg et al. (1985). However, direct verification of this hypothesis from observations is very difficult due to the sparse horizontal sampling. It is unclear from observations whether breaking of internal waves or wave-induced

* Additional affiliation: Department Atmospheric Sciences, University of California at Los Angeles, Los Angeles, California.

+ The National Center for Atmospheric Research is sponsored by the National Science Foundation.

Corresponding author address: Dr. Dailin Wang, National Center for Atmospheric Research, P.O. Box 3000, Boulder, CO 80307-3000. E-mail: wangd@ncar.ucar.edu

local shear instability is the primary cause of the deep turbulence cycle. It is also unclear from the observations whether the diurnal cycling of the mean gradient Richardson number is an intrinsic part of the equatorial ocean boundary layer. Peters et al. (1988) showed that the gradient Richardson number Ri has a diurnal cycle between 25 and 50 m for TH1. The shear was computed from acoustic Doppler current profiler (ADCP) data, which were collected below about 20 m. H. Peters (1996, personal communication) also found that the diurnal cycle of Ri also exists for the depth range 10–25 m when the shear is computed from data collected from current meter moorings. Nearby observations, however, did not reveal a diurnal cycle of Ri (Chereskin et al. 1986), although shear and stratification did show diurnal cycles separately. For the depth range of 10–25 m, their density fields must have been very different from that of Peters et al. because the same mooring data were used to compute the shear. TH2 (Peters et al. 1991) and TIWE (Lien et al. 1995) observations also reveal a diurnal cycle in the gradient Richardson number.

The temporal sampling (hourly) and vertical resolution (5 m) of turbulence measurements are adequate for the investigation of such questions. Unfortunately, the spatial sampling is not, since single-point vertical profiles are the usual measurement type. Therefore, as pointed by Peters et al. (1994), modeling efforts may be essential to understanding the mechanisms of the deep diurnal cycle of turbulence. Schudlich and Price (1992) attempted to model it by including the EUC, upwelling, and the zonal pressure gradient in a simple one-dimensional mixed layer model (Price et al. 1986). They successfully reproduced some observed aspects of the diurnal cycling boundary layer. Diagnostic calculations also showed strong diurnal cycle of turbulence dissipation well below mixed layer. The cause of the deep diurnal cycle of turbulence in their model is the interaction between convection, entrainment, and shear instability, modeled through three stability adjustments. They concluded that the presence of EUC is crucial for strong turbulence dissipation to occur below the mixed layer during nighttime convective cooling.

A potentially powerful modeling tool that can be applied to equatorial ocean boundary layer problems is large eddy simulation (LES). There have been some successes of applying LES to study equatorial oceanic turbulence (e.g., Wang et al. 1996; Skyllingstad et al. 1997, manuscript submitted to *J. Phys. Oceanogr.*) Its major advantage is that the energetic turbulent motions that contribute the most to the transfer of momentum and scalar quantities are explicitly resolved. Thus, there is relatively little sensitivity to the parameterization of the low-energy, subgrid-scale (SGS) motions. Instantaneous local Richardson number and horizontal mean Richardson number can be easily computed. This enables the behavior of Richardson number to be precisely examined during different phases of the diurnal cycle. Another advantage of an LES model over simple mixed layer and 1D boundary layer models is that three-dimensional internal waves are part of the solution, so their role in mixing can be addressed. The major limitation of LES is its computational requirement, which only allows us to use a horizontal domain size of typically 100 m $\times$ 100 m if we need to integrate the model for several days. Therefore, this study is limited by the fact that not all wavelengths of internal waves that might be contributing to the deep diurnal cycle of turbulence can be contained within the model domain.

Wang et al. (1996) studied diurnal cycling of the equatorial ocean boundary layer. They found it impossible for the local boundary layer to reach equilibrium because large-scale elements of equatorial dynamics, such as Ekman divergence and its associated upwelling, were excluded. Also, their LES solutions are not applicable to the study of deep-cycle turbulence because there was no EUC, as required by Schudlich and Price (1992). Therefore, in this LES study of the diurnal cycling boundary layer at the equator, the large-scale equatorial flow is allowed to influence the model resolved velocities and temperatures. The implementation of this physics is detailed in section 2, while other model specifics are contained in appendixes A, B, and C. Section 2 also has a description of the numerical experiments. In section 3 the degree of of equilibrium is assessed and the sensitivity of the LES solutions to horizontal resolution and domain size is presented. The diurnal cycle of turbulence at all depths in the model is presented and compared with observations in section 4. Section 5 is an investigation of the mechanisms responsible for the deep diurnal cycle of turbulence. Concluding remarks are presented in section 6, including a comparison of model eddy mixing coefficients with observational estimates.

2. Model description

The LES model used in this study was originally developed by Moeng (1984) and modified by P. Sullivan of the National Center for Atmospheric Research, Boulder, Colorado (Sullivan et al. 1996). The model employs a Fourier pseudospectral method in the horizontal and a second-order finite difference scheme in the vertical. The surface boundary conditions are flux type for momentum and temperature. The lower boundary conditions are radiation type to allow downward propagating internal waves to leave the system (Klemp and Durran 1983). The basic model has been modified for application to the equatorial ocean boundary layer. However, in this process study salinity is neglected. The most important development is the inclusion of the effects of the large-scale flow field, which has essential features of the equatorial upper-ocean dynamics. Computational constraints preclude the possibility of truly coupling the LES model with a general ocean circulation model. Therefore, a one-way interaction approach is adopted. The underlying assumption is the scale separation hypothesis, which states that the horizontal scales of the

equatorial large-scale flow are much larger than the scales of motions that are contained within the domain of the LES model, such that the horizontal derivatives of the large-scale terms are unaffected by the small-scale motions. We also assume the large-scale equatorial upwelling is unaffected by small-scale turbulence over the short time of an LES integration. We should point out that prescribing large-scale vertical velocity also means prescribing vertical mixing to some degree (McDougal 1984). So the one-way interaction approach is clearly flawed. However, the equatorial upwelling is mainly determined by the large-scale wind field through Ekman divergence and the profile used in this study is typical of the eastern equatorial Pacific. We do not see this as a major problem because the vertical divergence of turbulent fluxes does change as temperature and velocity evolve.

Another concern is the mesoscale eddy forcing terms. These terms can be computed from eddy-resolving ocean models (e.g., Gent and Cane 1989) and from observations (e.g., Bryden and Brady 1989). It is the evolution of mesoscale eddies as a function of space and time that cannot be straightforwardly applied to the model, so the associated forcing terms are prescribed. This procedure effectively removes the resolved scale turbulence from the coupling process.

The LES model equations for the prognostic variables $\mathbf{u} = (u, v, w)$ the resolved velocity, T the potential temperature, and e the subgrid turbulent kinetic energy (SGS TKE), then become

$$\mathbf{u}_t + \mathbf{u}\cdot\nabla\mathbf{u} + 2\boldsymbol{\Omega}\times\mathbf{u} = -\nabla p - \alpha\mathbf{g}T + \nabla\cdot\boldsymbol{\tau} + G, \quad (1)$$

$$\nabla\cdot\mathbf{u} = 0, \quad (2)$$

$$T_t + \mathbf{u}\cdot\nabla T = \nabla\cdot\mathbf{q} + \frac{1}{C_p}\partial_z I(t, z) + H_T, \quad (3)$$

$$e_t + \mathbf{u}\cdot\nabla e + We_z = \boldsymbol{\tau}:\nabla\mathbf{u} - \alpha g q_3 - \epsilon + \nabla\cdot 2\mathbf{K}\cdot\nabla e, \quad (4)$$

where $\boldsymbol{\Omega}$ is the earth's rotation vector, p is the pressure [a constant reference density is absorbed in p and $2e/3$ is added; see Moeng (1984)], g is gravitational acceleration, I is the solar radiation, $\mathbf{q} = (q_1, q_2, q_3)$ is the subgrid heat flux, $C_p = 4.1 \times 10^6$ J m^{-3} K^{-1} is the specific heat of seawater per unit volume, $\alpha = 0.00027$ K^{-1} is the thermal expansion coefficient, ϵ is turbulence dissipation, and $\mathbf{K}$ is the eddy viscosity tensor. The colon in (4) represents the inner product operator between two tensors. The parameterization of the unresolved subgrid Reynolds stress tensor τ and eddy viscosity tensor $\mathbf{K}$ are detailed in appendix A. We also include background diffusion near the core of EUC to stabilize the numerical integration (see appendix B). The initial profiles of the prognostic variables u and T are shown in Fig. 1a and Fig. 1b, respectively. The initial meridional and vertical velocity components are zero ($v = w = 0$) and the subgrid-scale turbulent kinetic energy is constant ($e = 10^{-8}$ m^2 s^{-2}) initially.

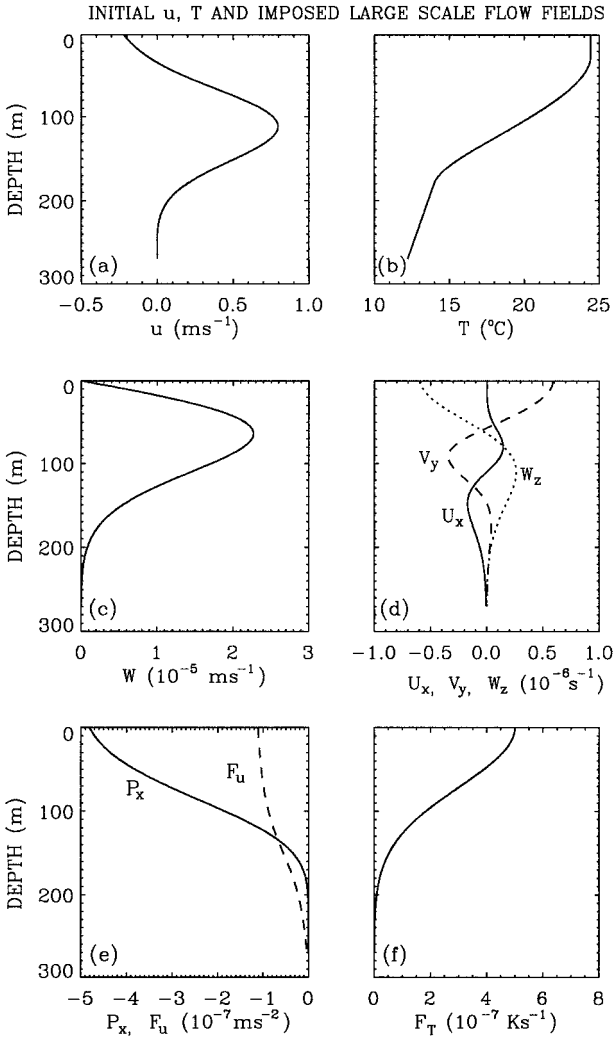

FIG. 1. Initial profiles of (a) zonal velocity, (b) temperature, (c) large-scale vertical velocity, (d) divergence, (e) zonal pressure gradient (solid line) and eddy forcing term in the zonal momentum equation (dashed line), and (f) eddy forcing term in the heat equation.

Equations (1)–(4) can be thought of as a Taylor expansion of a general circulation model at a point, with the large-scale terms and their horizontal derivatives independent of horizontal coordinates. For simplicity, we also assume these terms are independent of time. The large-scale interaction terms are $\mathbf{G}$ in (1), H_T in (3), and We_z in (4). The first of these is defined as

$$G_u = -uU_x - vU_y - Wu_z - P_x + F_u$$
$$G_v = -uV_x - vV_y - Wv_z - P_y + F_v$$
$$G_w = -uW_x - vW_y - Ww_z + F_w, \quad (5)$$

where U_x, U_y, V_x, V_y, W_x, and W_y are horizontal derivatives of the large-scale equatorial flow and W is the equatorial upwelling velocity. Higher-order terms in-

volving the large-scale flow gradients are neglected in (5). The large-scale flow satisfies the continuity equation

$$U_x + V_y + W_z = 0. \quad (6)$$

The prescribed profiles of W and each term in (6) are shown in Fig. 1c and Fig. 1d, respectively. All other horizontal derivatives of the large-scale flow are neglected:

$$U_y = V_x = W_x = W_y = 0. \quad (7)$$

Vector $\mathbf{F} = (F_u, F_v, F_w)$ represents mesoscale eddy forcing that is not explicitly contained in the LES model. We neglect the eddy forcing terms in the meridional and vertical momentum equations by choosing $F_v = F_w = 0$. Figure 1e shows the assumed profile of F_u, which remains constant in time.

The interaction term in the heat equation, H_T, is defined as

$$H_T = -u\hat{T}_x - v\hat{T}_y - WT_z + F_T, \quad (8)$$

where $\hat{T}_x$ and $\hat{T}_y$ are large-scale horizontal gradients of temperature, determined by the hydrostatic relations

$$\hat{T}_x = \frac{1}{\alpha g} P_{xz}$$

$$\hat{T}_y = \frac{1}{\alpha g} P_{yz}. \quad (9)$$

Meridional pressure variations are assumed to be negligible at the equator:

$$P_y = 0, \qquad \hat{T}_y = 0. \quad (10)$$

The profile of the zonal pressure gradient is shown in Fig. 1e (solid curve). The mesoscale eddy forcing of temperature is represented by F_T (Fig. 1f).

The expressions (u_z, v_z) and T_z in (5) and (8) are the total vertical derivatives of horizontal velocity and temperature. The vertical gradients of the prognostic variables, **u**, and T, of the LES model are not imposed. In deriving (5) and (8), turbulence is assumed to be horizontally homogeneous.

The large-scale terms of Fig. 1 are derived from a combination of the observational analysis of Bryden and Brady (1989) and a diagnosis from a modified version of the Pacific upper-ocean model of Gent and Cane (1989). The model employs the parameterization of Large et al. (1994) for vertical mixing. The model has 15 vertical levels (span over 400 m of the upper ocean). The zonal resolution is 110 km. The meridional resolution is variable and is about 25 km near the equator. We ran the model for three years after a 40-yr spinup with seasonal forcing (done by P. Gent and B. Kauffman at the National Center for Atmospheric Research, Boulder, Colorado) with frequent output. We then computed the annual mean balances, including the mesoscale eddy forcing terms. The large-scale terms are chosen to represent typical balances near 140°W on the equator.

It should be noted that if the LES model being used does not require horizontal periodicity, then large-scale terms such as U_x do not need to appear explicitly in the model equations. Instead, they appear in the form of lateral boundary conditions. However, such an approach has the drawback of dealing with open boundary conditions, so one needs to be careful to avoid wave reflections at the model boundary while imposing the vertical profiles of large-scale terms at the boundary. Moreover, fixing vertical profiles of velocity and temperature at the lateral boundaries would interfere with small-scale turbulent motions near the boundaries. Therefore either a very large model domain or relaxation type lateral boundary conditions will be needed to maintain the large-scale gradients. The advantage, however, is that the assumption of horizontal homogeneity of turbulence is not required.

The model is forced with a constant easterly wind stress of $\tau_x = -0.042$ N m^{-2}, which corresponds to a friction velocity of $\sqrt{|\tau_x|/\rho_0} = 0.0064$ m s^{-1} (where $\rho_0 = 1030$ kg m^{-3}) and a wind speed of about 5.4 m s^{-1}. The strength of this forcing is intermediate between the average over TH1 ($\tau_x = -0.071$ N m^{-2}) and over TH2 ($\tau_x = -0.019$ N m^{-2}). There is no meridional wind.

Diurnal surface heating and cooling is prescribed by two terms: a constant surface cooling of -200 W m^{-2} and solar radiation given by

$$I_s(t) = I_0 \sin(2\pi t - \pi/2)\mathcal{H}[\sin(2\pi t - \pi/2)], \quad (11)$$

where $I_0 = 776$ W m^{-2} is the local noon solar insolation, $\mathcal{H}$ is the Heaviside step function, and t is the time in days since midnight of day 1. Absorption of solar radiation $I(t, z)$ is prescribed for moderately clear type IB water (Jerlov 1968; Paulson and Simpson 1977);

$$I(t, z) = I_s(t)[\gamma \exp(z/\lambda_1) + (1 - \gamma) \exp(z/\lambda_2)], \quad (12)$$

where $\lambda_1 = 1$ m, $\lambda_2 = 17$ m, and $\gamma = 0.6$.

The daily averaged surface heating is $Q_0 = 47$ W m^{-2}, which is only about half of the average heating during either TH1 or TH2. The surface wind stress and net surface heat flux are consistent with the large-scale terms and the initial conditions of zonal velocity and temperature. In other words, the vertically integrated momentum and heat equations are balanced initially. Unfortunately, this balance cannot be maintained because of the evolution of **u** and T.

Computer resources place a severe constraint on the resolution and duration of LES integrations. We have chosen to integrate a base case (experiment I, see Table 1) for 6 days and then to use shorter integrations for exploring the sensitivity first to doubling the horizontal domain (experiment II), and second to halving the horizontal grid spacing (experiment III). Both of these integrations start from the solution of experiment I at 1500 local time of day 5 ($t = 4.625$ days) and run 33 hours through day 6 (to $t = 6.0$ days).

The specific parameters of these three experiments are catalogued in Table 1. All three have the same ver-

TABLE 1. Numerical experiments. The horizontal domain of the model is $L \times L$, with a $N_x \times N_y$ grid.

Experiment	L(m)	$N_x = N_y$	Initial condition	Integration length (h)
I	80	16	Fig. 1	144
II	160	32	Hour 111 of expt I	33
III	80	32	Hour 111 of expt I	33

tical resolution of 1 m and extend from the surface to 270-m depth. Exploratory integrations with coarser (2 and 3 m) vertical resolution show considerably more noise. As we shall see later, vertical resolution of 1 m only marginally resolves the entrainment layer. In experiment I, there are 16 × 16 grid points in the horizontal spanning 80 m × 80 m, with a grid spacing of 5 m. Some small divergence-free random noise was initially added in the top 6 levels to instigate the turbulence. Experiment II has the same 5-m grid horizontal spacing, but spans 160 m × 160 m with 32 × 32 grid points in each horizontal dimension. The initial condition for experiment II is constructed by mirroring the experiment I solution into the three additional quadrants of the expanded domain. Then some small random noise is added in the top 6 levels in order to break the symmetry and to obtain a nontrivial solution. Experiment III has the same domain size of experiment I, but the greater number of grid points of experiment II, and hence the finest horizontal resolution of 2.5 m. Its initial condition is a linear interpolation of the experiment I solution. The last 24 hours of the integration for all three experiments will be compared and referred to as day 6 ($t = 5.0$ days to $t = 6.0$ days).

3. Assessment of day 6 solutions

The inclusion of large-scale terms is necessary for the LES model to reach equilibrium, but the necessary surface stress and heat flux for the prescribed large-scale flow are not known. Two possible ways of reaching a true equilibrium solution are allowing the large-scale terms to evolve (two-way interactions) and extensive iteration. Since neither options is computationally feasible, we must be content with the degree of equilibrium reached by day 6.

Figure 2 shows the time–depth sections of temperature and zonal velocity for experiment I. The solution is clearly much nearer equilibrium than when the equatorial large-scale terms are not included (compare to Fig. 3 of Wang et al. 1996). Even though the thermocline is still deepening slowly on day 6, the mixed layer depth (defined by the depth at which potential density differs from that of the surface by 0.01 kg m^{-3}) shows very steady diurnal cycle for $t > 2.0$ days (dashed lines in Fig. 2). The surface westward current also shows a very steady diurnal cycle (Fig. 2b). However, the equatorial undercurrent is accelerating due to the zonal pressure gradient and local imbalance of the initial field. The depth of turbulent entrainment is evident in the convergence of contour lines between 60 and 100 m in Fig. 2b. The EUC acceleration is confined to below this depth; in other words, the EUC acceleration stops when it is entrained into the turbulent boundary layer. The important feature is that at the depths of interest (above about 60 m) the diurnal cycles of days 5 and 6 are nearly identical.

Figure 3 shows daily averaged balances of the zonal momentum and the heat equations for days 2 and 6 of experiment 1. Even though on day 6 the time tendency terms (u_t and T_t) are nonzero, showing a degree of disequilibrium, they are generally smaller than other terms (e.g., pressure gradient and vertical divergence of heat flux, respectively) in the boundary layer above 80 m. This feature is especially true for the momentum equation, where the time rate of change (refer to solid line in Fig. 3c) is comparatively small everywhere except at the bottom of the boundary layer, which is characterized by a sharp gradient in the vertical derivative of turbulent stress (dash–dotted lines). Even though the time rate of change in the heat equation is not dominant, it is still significant at all depths. Thus, only limited success was achieved in obtaining an equilibrium solution. It should be noted that without the large-scale terms the time rates of change would be exactly equal to the vertical divergence of turbulent fluxes. With such a balance the westward surface current would be accelerating without bound and there would be no mechanism to stop the deepening of the thermocline. Inclusion of the large-scale equatorial terms are, therefore, beneficial in obtaining a solution with acceptably small trends.

The day 6 mean profiles of u and T from the three experiments are nearly indistinguishable (not shown), but there are some significant quantitative differences in turbulent measures. Figure 4 compares day 6 mean vertical profiles of total turbulent kinetic energy (TKE), dissipation, momentum flux, and heat flux. TKE shows the largest differences among the three experiments. Turbulent activity tends to be highest in experiment II, and lowest in experiment III. The increase of turbulent kinetic energy and fluxes for experiment II is perhaps because the larger domain can contain larger eddies. The decrease of turbulent kinetic energy and fluxes for experiment III may be partly due to the initialization procedure. In setting up experiment III, the linear interpolation to the finer horizontal grid neither excites kinetic energy at the newly resolved scales, nor decreases subgrid-scale turbulent kinetic energy. Thus, experiment III starts with a too high level of subgrid-scale kinetic energy (i.e., more viscosity) and a too low level of resolved kinetic energy. The integration may be too short to overcome these initialization problems. Thus,

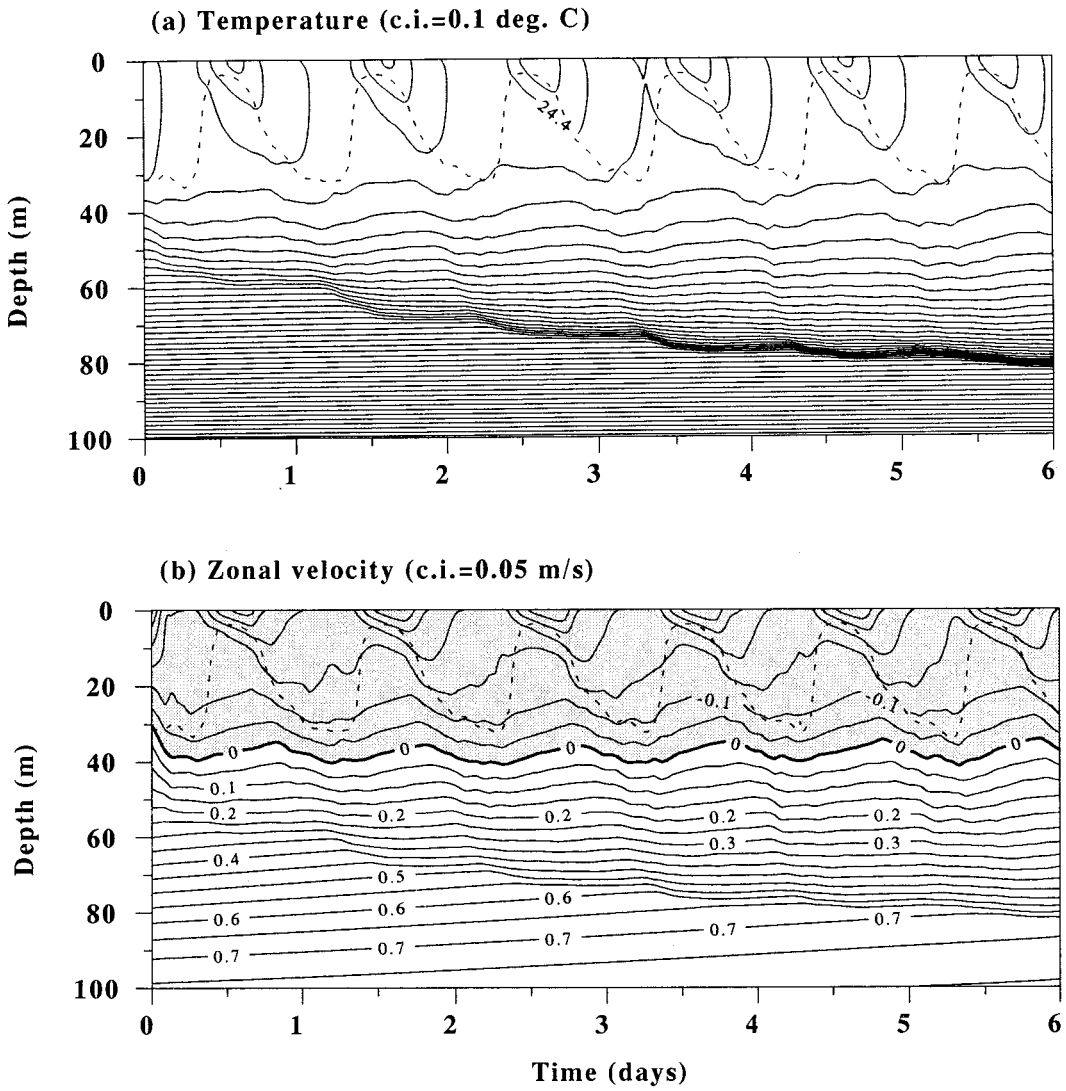

FIG. 2. Experiment I: (a) Hourly mean of horizontally averaged temperature. (b) Zonal velocity. Dashed lines indicate the depth of mixed layer. The depth of the mixed layer is defined as the depth at which density differs from that of the surface by 0.01 kg m^{-3}.

the most physical solutions appear to be those of experiment II, and hereafter we will present only the results of experiment II, unless explicitly noted otherwise.

Figure 5 compares the last 33 hours of three turbulent quantities at $z = 40$ m. That experiment I has the fewest horizontal grid points is readily apparent in the strong fluctuations of turbulent momentum and heat fluxes (solid lines in Fig. 5). These fluctuations are due to the fact that too few turbulent eddies are sampled at any one time. This aliasing is not as severe above $z = 20$ m (not shown). When the time series are filtered with a 6-h running average, the three experiments qualitatively agree. This agreement and the intermediate turbulent activity suggest that when resources are limited, a coarse horizontal resolution LES integration like experiment I may produce useful, though not ideal, solutions.

Figure 6 shows the diurnal variation of temperature and zonal velocity for day 6 of experiment II. The diurnal variation of surface temperature and velocity are 0.25°C and 0.16 m s^{-1}, respectively. The amplitudes of the diurnal cycle decrease with depth. For example, at 40 m, the diurnal variation of temperature and velocity are 0.07°C and 0.05 m s^{-1}, respectively. The dense contours near 80 m reflect the facts that the system is not in equilibrium; that is, the erosion of thermocline is continuing. Figure 6 also shows the diurnal cycle of mixed layer depth (dashed curve). From a minimum of about 5 m during the day the mixed layer deepens to about 30 m late at night. A striking feature is the asymmetry between the slow deepening and rapid shallowing. The maximum rate of shallowing is 16 m h^{-1} between 0800 and 0900. The deepening rate is approxi-

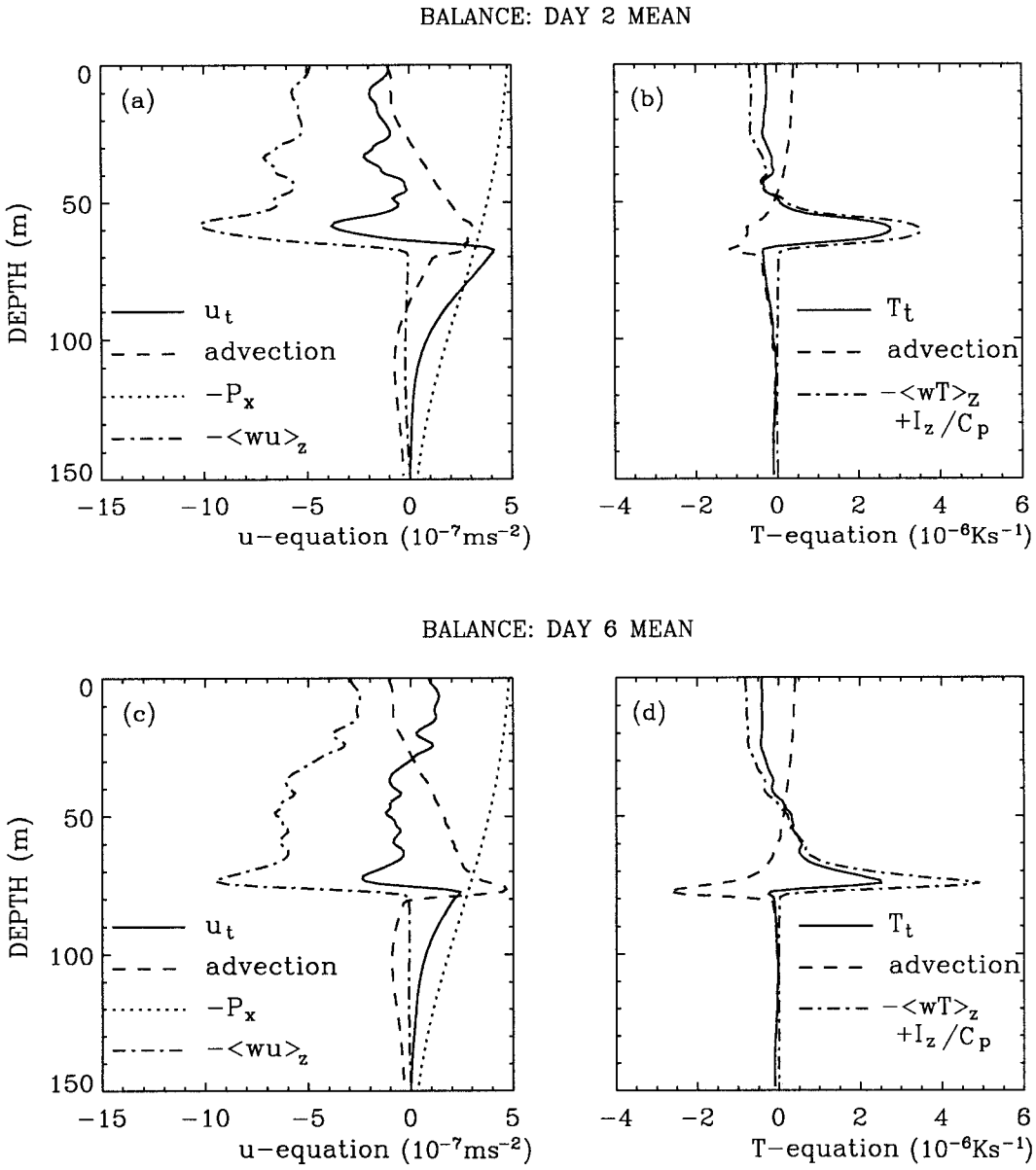

FIG. 3. Time-averaged balances in the zonal momentum and heat equations for day 2 and day 6 of experiment I. Solid lines: time rate of change; dashed lines: advection = $-uU_x - vU_y - Wu_z + F_u$ for momentum and advection = $-u\overline{T}_x - v\overline{T}_y - WT_z + F_T$ for heat; dotted lines: zonal pressure gradient; dash–dotted lines: vertical divergence of turbulent momentum flux and heat flux with solar heat flux being included. Note that the mesoscale eddy forcing terms are included in the advection terms.

mately steady at only 5 m h^{-1} following the onset of nighttime convection at about 1800. The 3:1 ratio of shallowing to deepening rate agrees with the observations of Lien et al. (1996) for the days when nighttime mixed layer depth is about 30 m.

4. The diurnal cycle of turbulence

The modeled diurnal cycle of turbulence dissipation (Fig. 7a) bears a strong resemblance to observations. For example, Lien et al. (1995) show that during the first 6 days of their observations, when the nighttime mixed layer depth was about 30 m, there was strong dissipation ($\epsilon > 10^{-7}$ m^2 s^{-3}) penetrating to 80-m depth and weak dissipation (as small as $\epsilon < 10^{-8}$ m^2 s^{-3}) during the day just below the daytime mixed layer. They also find the largest diurnal cycle of dissipation to be at about 20-m depth, but show less than an order of magnitude night to day difference at 60-m depth. There were similar mixed layer depths during Tropic Heat I (November 1984) and the ensemble averages of Moum et al. (1989) shows a region of strong dissipation deep-

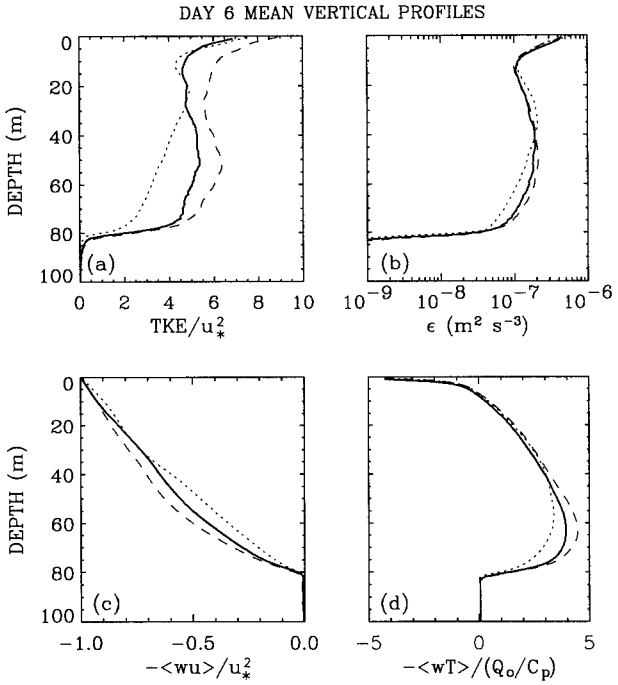

FIG. 4. Day 6 mean (a) turbulent kinetic energy, (b) dissipation, (c) turbulent momentum flux, and (d) turbulent heat flux for experiments I (solid), II (dashed), and III (dotted). Angle brackets represent ensemble average (1-day mean of horizontal average).

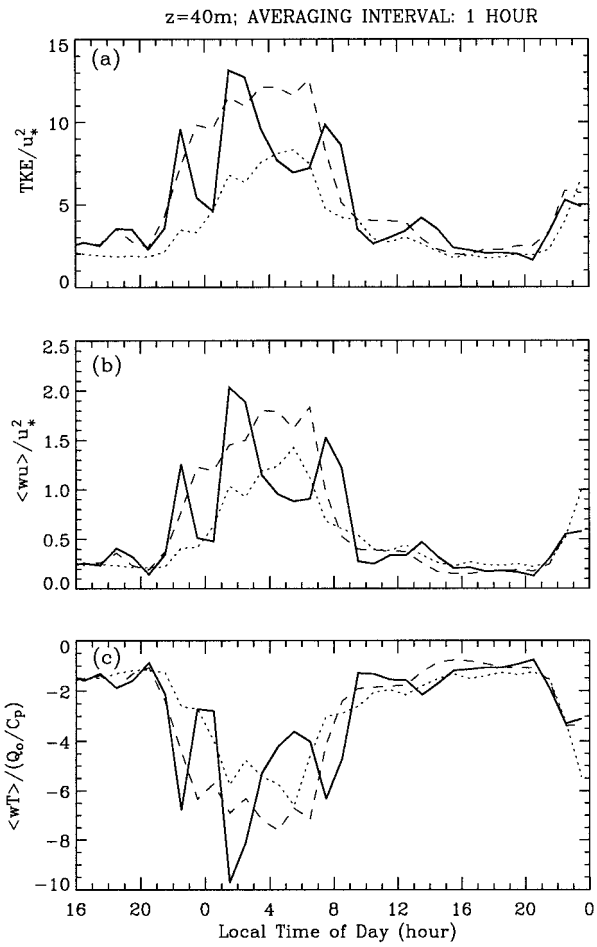

FIG. 5. Diurnal cycle of (a) horizontal mean turbulent kinetic energy, (b) turbulent momentum flux, and (c) turbulent heat flux, at 40 m, for experiments I (solid lines), II (dashed lines), and III (dotted lines). The time series are taken from the last 33 hours of the integration of the three experiments. Here $u_{at} = 0.0064$ m s^{-1}, $Q_O = 47$ W m^{-2} is the daily averaged equivalent surface heat flux, and $C_p = 4.1 \times 10^6$ J m^{-3} K^{-1} is the specific heat of seawater per unit volume. Angle brackets represent ensemble average (1-h mean of horizontal average).

ening from about 20 m at sunset to about 70 m at sunrise. These averages do show a well-defined diurnal cycle with more than an order of magnitude day to night difference between 20 and 80 m. The above degree of agreement depends critically on the presence of an EUC in the model. Figure 7b shows the diurnal cycle of turbulence dissipation in the absence of an EUC, corresponding to day 4 of case A2 in Wang et al. (1996, Fig. 4). The effects of the EUC are most evident below about 20-m depth. With an EUC (Fig. 7a) strong dissipation penetrates to 80 m, or 50 m deeper than the mixed layer depth (indicated by the dashed line). Without an EUC this strong dissipation is found only above 45 m, just 15 m deeper than the mixed layer depth.

It is interesting to note the asymmetry of decaying and growing of turbulence dissipation just below the mixed layer (Fig. 7a, about 20 m). The growing rate is about 3 times the decay rate, a feature just the opposite to the mixed layer shallowing and deepening rate. This means the decay of turbulence in the absence of convective forcing is a slower process than the growth of turbulence when convective cooling is switched on.

Figure 8 shows the LES diurnal cycles of turbulent momentum and heat fluxes, normalized by u_*^2 and Q_0/C_p, respectively. The maximum momentum flux of about $2.2u_*^2$ occurs at about 20-m depth near midnight ($t = 0$ h). A local momentum flux of more than twice the surface value set by the prescribed wind stress is due to nocturnal convective cooling. Therefore, there is a strong day and night difference in the momentum flux below the mixed layer. From 1000 to 1600, the momentum flux below the mixed layer is near zero, with remnants of slowly decaying nighttime turbulence evident below 40 m. The turbulent heat flux has a similar diurnal cycle at depth. There is a large diurnal variation, with maximum variation of about $8Q_0$ or 376 W m^{-2}, occurring at 70 m (Fig. 8b).

The budget of total (resolved plus subgrid) TKE is

$$\frac{d}{dt}(\text{TKE}) = \mathcal{S} + \mathcal{T} + \mathcal{P} - \mathcal{B} - \epsilon + (\text{advection of TKE by large-scale flow}), \quad (13)$$

where the first five terms on the right-hand side represent

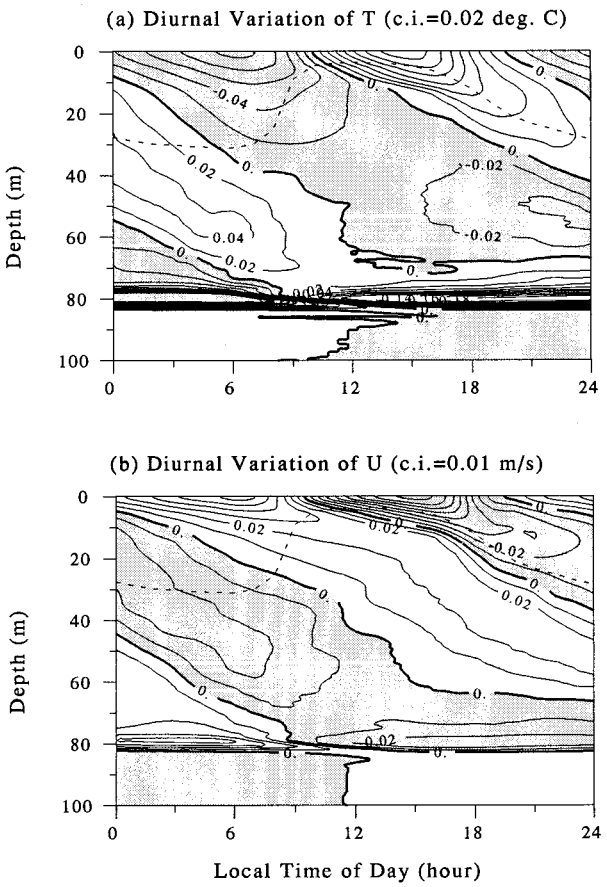

FIG. 6. Diurnal variation of (a) temperature and (b) zonal velocity for experiment II, with daily averages removed. Negative valued regions are shaded. Dashed lines indicate the depth of the mixed layer.

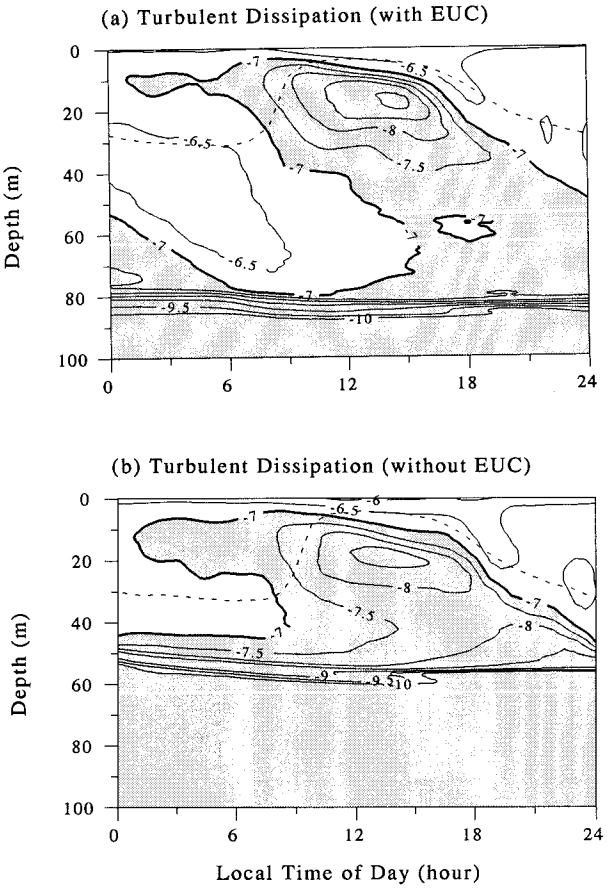

FIG. 7. Diurnal cycle of turbulence dissipation in $\log_{10}[\epsilon/(\mathrm{m}^2\ \mathrm{s}^{-3})]$ scale (a) with EUC and (b) without EUC. Dashed lines indicate the depth of mixed layer. Regions with dissipation less than $10^{-7}\ \mathrm{m}^2\ \mathrm{s}^{-3}$ are shaded.

shear production ($\mathcal{S}$), divergence of the vertical flux or turbulent transport ($\mathcal{T}$), work done by fluctuating pressure ($\mathcal{P}$), buoyant suppression/production ($\mathcal{B}$), of TKE, and dissipation (ϵ), respectively. Advection of TKE by large-scale flows is negligible (see appendix C for details). This is in contrast to the importance of large-scale advection in the momentum and heat equations. The diurnal cycle of this budget is presented in Fig. 9 as averages over four time periods: 0400–1000, 1000–1600, 1600–2200, and 2200–0400. The primary balance throughout the boundary layer is between shear production $\mathcal{S}$ (dashed lines) and dissipation ϵ (thick dotted lines), but $\mathcal{B}$ (dash–dotted lines) is often not negligible especially between 20 and 80 m during the day. Shear production and dissipation are strongest for the time period of 0400–2200 and weakest for 1600–2200 at depth, respectively. The time rate of change (thin dotted line) is very small compared to other terms such as shear production $\mathcal{S}$.

Figure 10 shows temperature gradient variance, normalized by the square of the horizontal mean of the vertical gradient of temperature, at various times of the day. Temperature (Fig. 2) shows significant diurnal variation above 30 m, but a weak diurnal cycle below. That the normalized temperature gradient variance is always larger than unity above 70 m (well below the mixed layer depth, which varies between 5 and 30 m) is indicative of strong nonlinearity of motions in the LES model. We also found that there are no systematic phase propagations relative to the mean current in both the horizontal plane and in the vertical direction. The typical timescale (the timescale over which vertical velocity w changes sign) and vertical length scale (the vertical distance over which w changes sign) in the entrainment layer (60–80 m) are about 1 min and 2–10 m. Therefore, motions below the mixed layer are more turbulence-like than wavelike. Observations (e.g., McPhaden and Peters 1992; Lien et al. 1995) seem to suggest that the typical wavelength of the internal waves below the mixed layer is 160–300 m. Our model domain is not large enough to resolve these waves well. Nevertheless, the LES model was able to capture the main features of the deep diurnal cycle turbulence.

The diurnal cycle of turbulence dissipation at depths

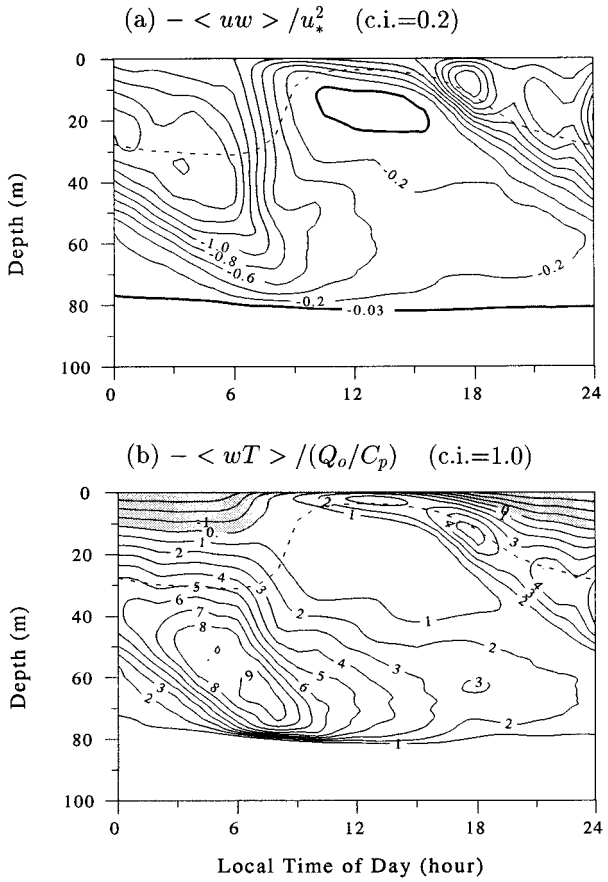

FIG. 8. Diurnal cycle of (a) momentum flux and (b) heat flux for experiment II. Dashed lines indicate the depth of mixed layer. Momentum flux and heat flux are normalized by friction velocity squared and daily mean surface heat flux, respectively.

20, 40, and 60 m for the three LES experiments are compared to ensemble averaged observations in Fig. 11. The two sets of Tropic Heat I (TH1) results (Moum et al. 1989: plus signs; Peters et al. 1994: squares) are based on measurements coincident in time and from ships only 10 km apart. Nevertheless, there are significant differences.

As noted by Peters et al. (1994), mean and nocturnal dissipation rates were lower in TH2 (triangles, Fig. 11) due to a weaker EUC, stronger stratification, and weaker winds. As a result, the nighttime maximum mixed layer depth was 36 m in TH1 and only 20 m in TH2. Therefore, the LES experiments (Fig. 11) is more comparable to TH1. The Lien et al. (1995) results (crosses) are also comparable because they are from the earlier half of their observations when the nighttime mixed layer depth averaged about 35 m. At both 40 and 60 m, there is qualitative agreement between the LES experiment II diurnal cycles and the combined Moum et al. (1989) and Lien et al. (1995) observations. The diurnal cycles peak at around sunrise ($t = 6$ h), and their minima occur between 1600 ($t = 16$ h) and midnight ($t = 24$ h). The largest systematic difference is the low LES dissipation rates at 20 m, especially around noon. Even though corresponding daily values observed by Lien et al. (1995) are in the range $10^{-9}\ \mathrm{m^2\ s^{-3}} < \epsilon < 10^{-7}\ \mathrm{m^2\ s^{-3}}$, a probable cause is numerical. The dominant eddy scale is highly variable and becomes smaller as the surface forcing becomes more stable and as the surface is approached. Therefore, $z = -20$ m and $t = 12$ to 15 h is a region and time of relatively poor LES resolution. In this situation there is an overreliance on the SGS parameterization and too little turbulent activity. This view is supported by the larger dissipation rates in the higher resolution of experiment III compared to the other experiments (refer to the top panel of Fig. 11).

5. The mechanics of the deep diurnal cycle turbulence

We have found that the gradient Richardson number of the large-scale horizontal flow,[1]

$$\mathrm{Ri}^L = \langle N^2 \rangle / \langle u_z \rangle^2, \tag{14}$$

shows a diurnal cycle within the mixed layer as well as below the mixed layer (left panels of Fig. 12). There are also related diurnal cycles in the distributions of local (pointwise) gradient Richardson number (right panels of Fig. 12). The local Richardson numbers have been distributed into three groups: gravitationally unstable points (solid lines, local Ri < 0), gravitationally stable but dynamically unstable points based on the shear instability criterion of $0 <$ (local Ri) < 0.25 (dashed lines), and stable points (dotted lines, local Ri > 0.25). At 1 m, there are virtually no stable points, with gravitational instability dominating at night and dynamical instability during the day. There is a similar cycle of Ri^L, whose values range from -0.3 at night to 0.03 around noon.

At 20 m, all three local Richardson number categories show very strong diurnal cycles. At night 70% of the points are unstable (i.e., local Ri < 0.25) and during the day as many as 80% of the points are stable. The corresponding Ri^L varies from 0.23 at midnight to 0.90 at 1500. The amplitude of this diurnal cycle decreases as the depth increases. At 40 m it is 0.25 to 0.40 with a similar phase. This diurnal cycle results from an in phase night to day variation in the percentage of stable points (dotted line, Fig. 12h) from 25% to 50%. At 40 m and below the number of gravitationally unstable points remains relatively constant around 15%, an indication that strong nighttime turbulence at these depths is initiated primarily by the increase of local shear rather than the breaking of internal waves (overturning wave instability) in the model. At 60 m there is a phase change in those weak diurnal

[1] Gradient Richardson number of the large-scale flow (Ri^L) refers to the gradient Richardson number computed from horizontally averaged shear and stratification. For brevity, we will call it mean Ri, or simply Ri when confusion shall not arise. Local Richardson number (or local Ri) means the gradient Richardson number computed from local (pointwise) shear and stratification.

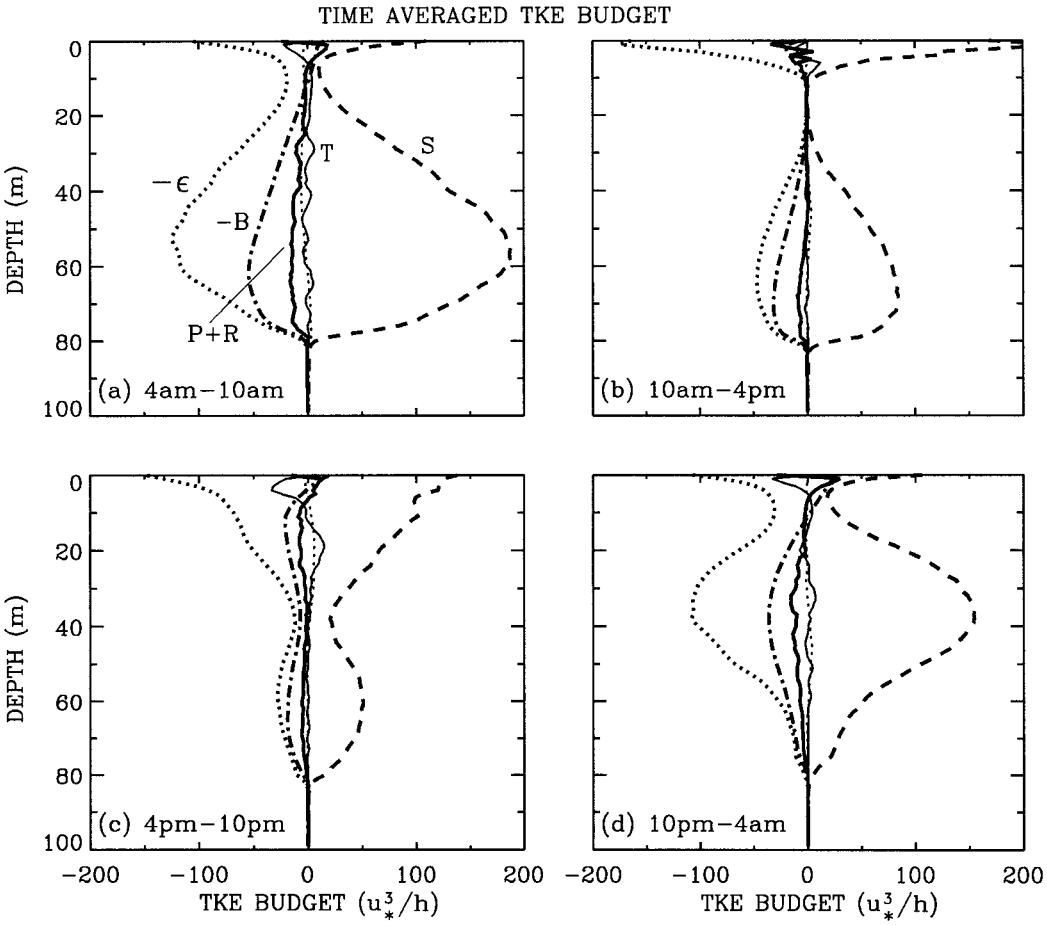

FIG. 9. Budget of turbulent kinetic energy (TKE) for four local time periods: (a) 0400–1000, (b) 1000–1600, (c) 1600–2200, and (d) 2200–0400. $\mathcal{S}$ is shear production (dashed lines), $\mathcal{B}$ is buoyant suppression (dash–dotted lines), ϵ is turbulence dissipation (thick dotted lines), $\mathcal{T}$ is turbulent transport (or turbulent diffusion) (thin solid lines), $P + R$ is the sum of work done by fluctuating pressure and truncation error (thick solid lines). Thin dotted lines are the time rates of change of TKE. The advection of TKE by large-scale flows is an order of magnitude smaller than the time rate of change and therefore is not shown. The pressure redistribution term is not computed directly from velocity and pressure fields, but by method of subtraction. So it contains truncation errors (denoted by R in Fig. 9a).

cycles that are evident. Here Ri^L changes from 0.30 at 0600 to about 0.43 at midnight, and there is a minimum in the number of stable points at about 0800. At 70 m Ri^L changes from 0.36 at 0800 to about 0.47 at midnight. In contrast to 40 and 60 m, the number of gravitationally unstable points at 70 m do show a diurnal cycle (Fig. 12j). If the resolution of the LES model is fine enough, one would expect to see diurnal cycles of the number of gravitationally unstable points at 40 and 60 m as well. In other words, the diurnal cycle of ''wave overturning'' below the mixed layer occurs at scales comparable to or smaller than the grid sizes of the LES model. We computed the skewness of resolved zonal temperature derivative and found it shows a diurnal cycle at all depths (varies by a factor of about 10). This is an indication of increased tendency of wave overturning at night. However, the values of the resolved skewness are much smaller than that of laboratory experiments of stratified shear flows. One possible reason is that we do not have an estimate of the subgrid-scale skewness. We suspect that as depth increases, the wave overturning occurs at decreasing length scales because of the increase in stratification. So even our finest resolution of 2.5 m $\times$ 2.5 m $\times$ 1 m is not enough to resolve wave overturning well below the mixed layer.

The most revealing correlation is between the maximum daily turbulent dissipation (Fig. 7a) and the maximum number of dynamically unstable points (Figs. 12g–j, dashed lines). These maxima occur before midnight at 20 m, just after midnight at 40 m, about sunrise at 60 m, and between 0700 and 0800 at 70 m. This correlation suggests that the diurnal cycle of turbulence dissipation in the model is caused by increased local dynamic instability. In order to explore this mechanism more fully, we now examine three relationships of distributions: gravitational to dynamic instability, stratification to shear, and Richardson number to SGS TKE.

First, Fig. 13 contours instantaneous Brunt–Väisälä frequency squared at the section $y = 80$ m at 0600 on

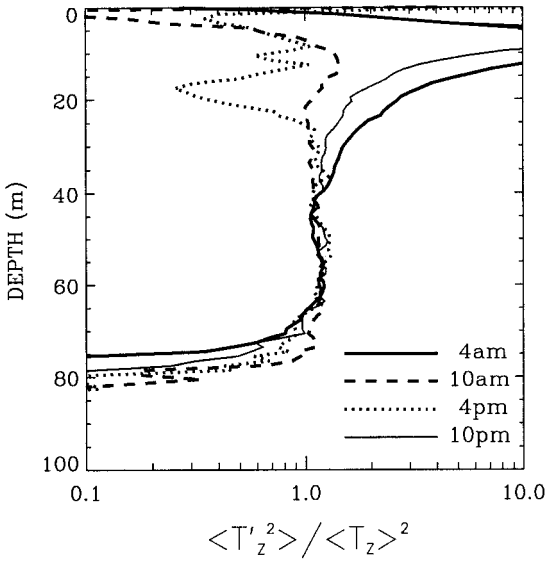

FIG. 10. Temperature gradient variance normalized by the horizontal mean temperature gradient squared at various times of the day. Angle brackets represent ensemble average (1-h mean of horizontal average).

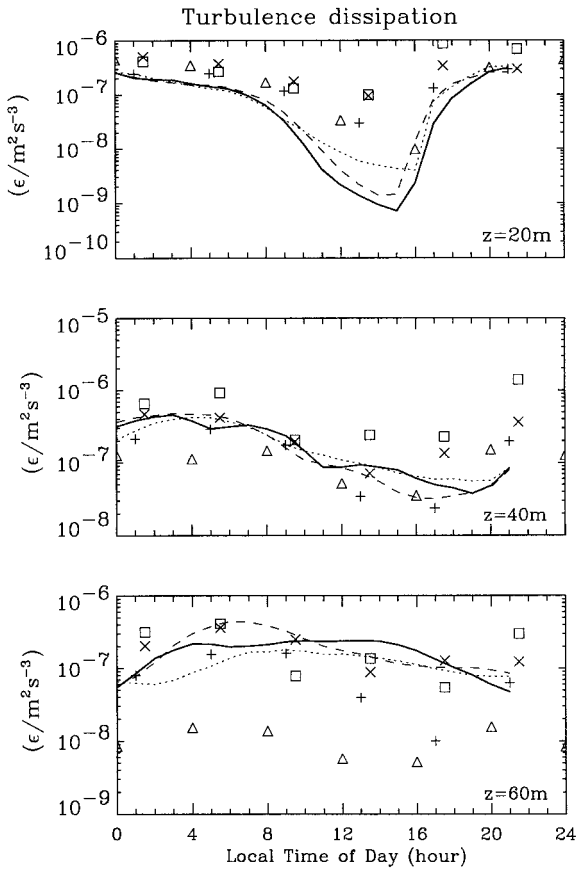

FIG. 11. Diurnal cycle of turbulence dissipation for experiments I (solid), II (dashed), and III (dotted) at $z = 20$ m (top panel), (b) $z = 40$ m (middle panel), and (c) $z = 60$ m (bottom panel), filtered with a 4-h running average. Also plotted are ensemble 4-h averages of Tropical Heat I (plus signs: Moum et al. 1989; squares: Peters et al. 1994), Tropical Heat II (triangles: Peters et al. 1994), and TIWE (crosses: Lien et al. 1995, from days with shallow mixed layers only).

day 6 of experiment II. Regions of stable stratification ($N^2 > 0$) are shaded. In addition, locations of local dynamic instability ($0 <$ local Ri < 0.25) are indicated by plus symbols. In order to emphasize the large-scale structures, both temperature and horizontal velocity were smoothed with two passes of a [1/4, 2/4, 1/4] filter in the vertical before the computation of local N^2 and local Ri. The vertical scales of the gravitationally unstable (clear) regions decreases as depth increases. This scale can be as large as 20 m near the surface, but as small as 2–3 m at depth, an indication that our vertical resolution of 1 m is marginally adequate to resolve the overturnings of interest. This zonal section reveals that at the depth (about 60 m) of maximum turbulence dissipation (Fig. 7a), and heat flux (Fig. 8b), there are few gravitationally unstable (overturning) regions, but a concentration of locations of dynamic instability.

Second, Fig. 14 shows the probability density function for the depth range 50–70 m at 0600 in the space of N^2 and vertical shear of horizontal velocity, S_h, defined as

$$S_h = u_z^2 + v_z^2.$$

The ratio of the two normalizing factors $\langle N^2 \rangle : \langle S_h \rangle$ is about 1:4. Therefore, a straight line through the origin with slope n, corresponds to a local Richardson number, Ri, of $0.25n$. The dashed lines represent local Ri = 0.0, 0.25, and 1.0. Most points lie in the stable range $0.25 <$ local Ri < 0.50. A significant number of points are found to be dynamically unstable, but most of these are near local Ri = 0.25 and few are in the region $0.0 <$ local Ri < 0.10. This distribution suggests that, as a point moves from the stable regime to be dynamically unstable, it generates turbulence while Ri is still near 0.25, and in so doing the point becomes stable again.

Finally, in the above scenario the turbulence generation would be seen as high values of subgrid turbulent kinetic energy ($e \propto \epsilon^{2/3}$), and hence dissipation. This relationship is supported by Fig. 15, a scatterplot of local Ri versus subgrid turbulent kinetic energy from all points between 50 and 70 m, again at 0600. The highest values of SGS TKE are indeed associated with dynamic instability, and tend to occur in the range $0 <$ local Ri < 0.25. Not only are there relatively few gravitationally unstable points, but these overturnings do not coincide with high levels of SGS TKE, and hence ϵ. Very stable points (local Ri > 0.5) also have low SGS TKE.

6. Discussion and conclusions

As pointed out in Wang et al. (1996), equatorial large-scale flows have to be included in an equatorial ocean boundary layer model to achieve equilibrium. To ad-

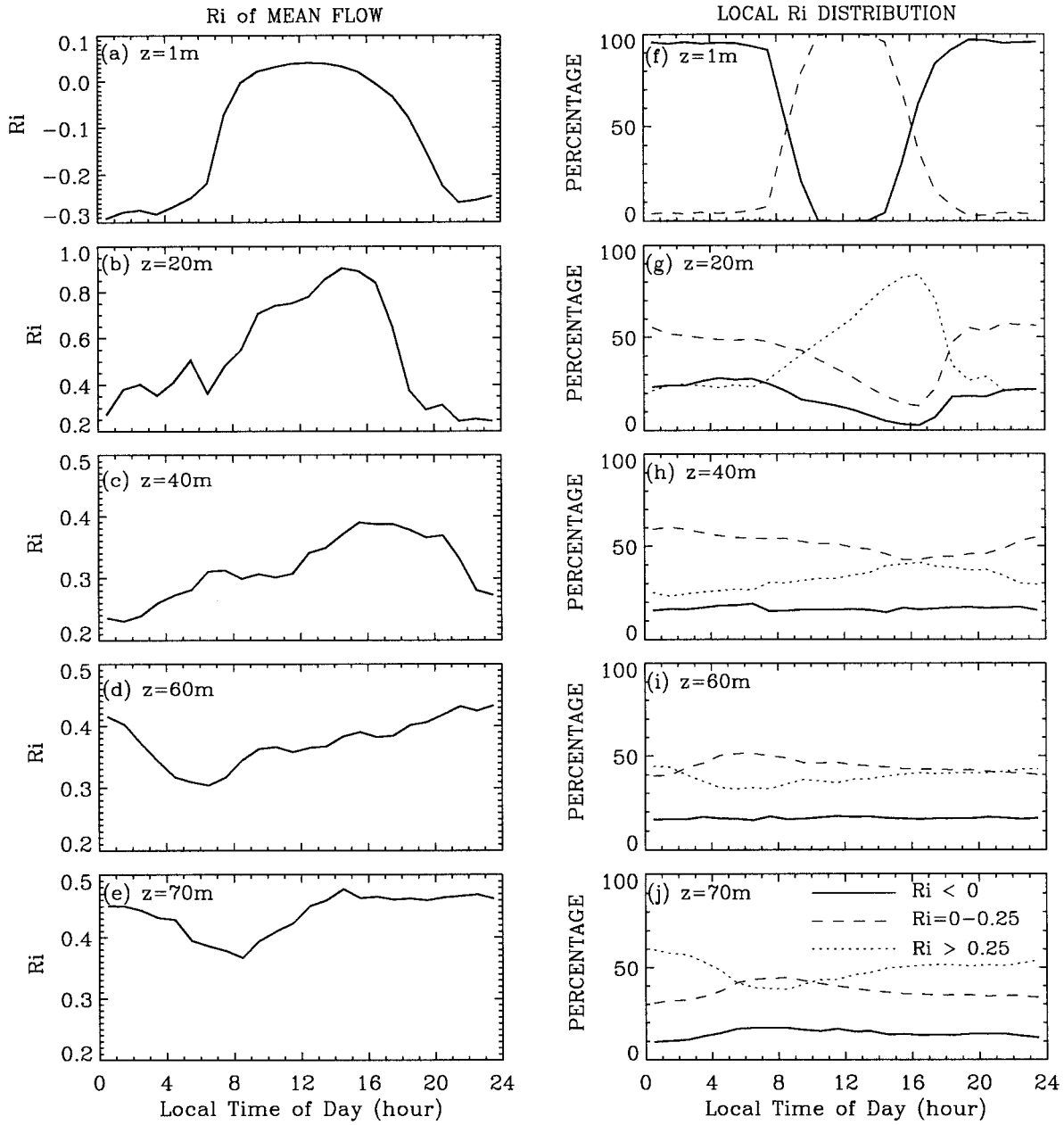

FIG. 12. Diurnal variation of mean gradient and local Richardson numbers. The mean gradient Richardson number is computed from the horizontal averages of velocity and temperature [see Eq. (14)], while the instantaneous local Ri is computed at every grid point of the model domain. Mean gradient Richardson number is shown at the left panels (a)–(e) and the local R_i is shown at the right panels (f)–(j). The solid, dashed, and dotted lines represent the percentages of points with Ri $<$ 0, Ri = [0, Ri_c], and Ri $>$ Ri_c, respectively. Here, Ri_c = 0.25. We have tried Ri_c = 0.2 and the results are qualitatively the same.

dress this issue, we included zonal pressure gradient, equatorial upwelling, horizontal divergence, zonal gradient of temperature, and mesoscale eddy forcing terms in a LES model. After 6 days of integration an acceptable degree of equilibrium is achieved, with the tendency term in the momentum equation much smaller than other terms, at least over the top 60 m. Most importantly, the acceleration of the westward surface current is not unbounded, as in Wang et al. (1996). The acceleration of the eastward flowing EUC is also greatly reduced by day 6. The tendency term in the heat equation is only about half the divergence of turbulence flux. The inclusion of large-scale terms in the heat equation proves to be beneficial, even though absolute equilibrium is not achieved within 6 days. Without these terms the time rate of change would be exactly equal to the divergence of turbulent heat fluxes, an unrealistic balance in the equatorial upper ocean, at least for the east-

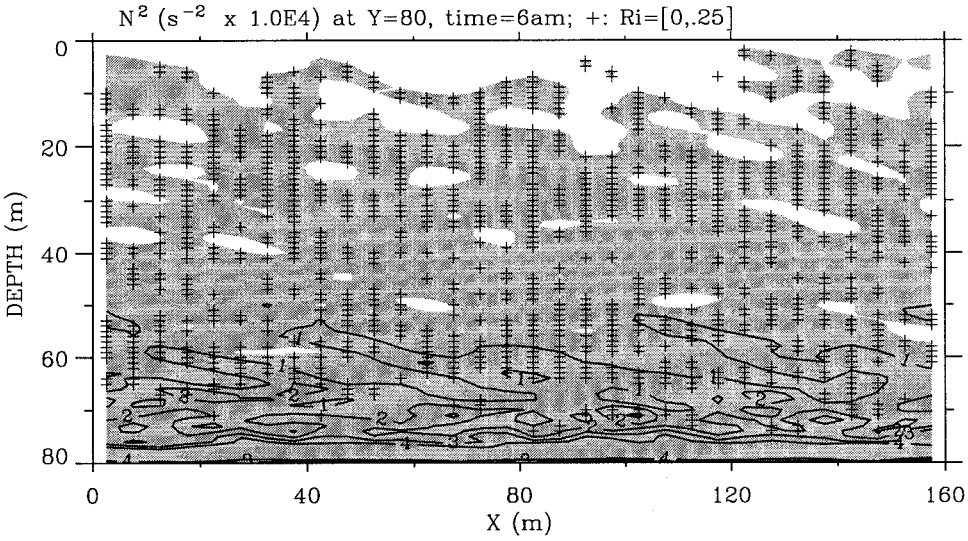

FIG. 13. Instantaneous stratification at 0600 and at $y = 80$ m experiment II. Gravitationally stable regions are shaded. The plus signs indicate points with local Ri in the interval [0, 0.25]. The temperature is smoothed vertically with two passes of the filter [1/4, 2/4, 1/4] before the N^2 is computed.

ern Pacific. A certain way of achieving true equilibrium is to allow two-way interactions where the large-scale flow adjusts to the changes of small-scale processes. This type of model is not feasible in the near future due to the limitation of computer resources. However, better equilibria might be achieved with some iteration, namely, using the LES results to refine the parameterization of vertical fluxes for ocean circulation models, which in turn, will provide improved large-scale terms used in the LES model.

It should not be surprising that turbulence exists below the mixed layer because the depth of mixed layer is not necessarily the depth of the boundary layer. However, high levels of turbulence are found at depths more than twice the mixed layer depth. This discovery was indeed a surprise (Gregg et al. 1985; Moum and Caldwell 1985). Several hypotheses have been proposed in

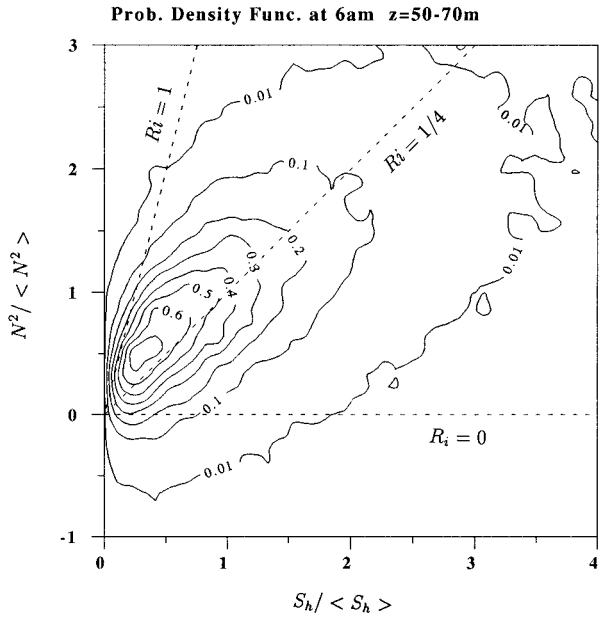

FIG. 14. Probability density function for the depth range 50–70 m at 0600. The Brunt–Väisälä frequency squared (N^2) and the shear squared ($S_h = u_z^2 + v_z^2$) are normalized by their corresponding means. The ratio $\langle N^2\rangle/\langle V_z^2\rangle$ is about 1/4.

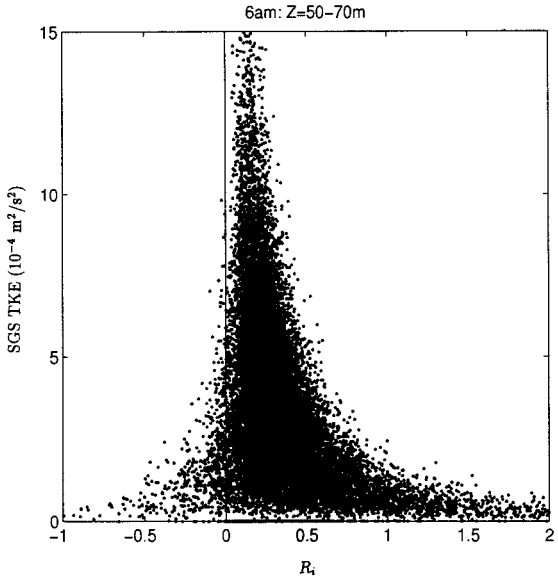

FIG. 15. Scatterplot of local Richardson number vs subgrid-scale turbulent kinetic energy for the depth range 50–70 m at 0600 local time for experiment II. Temperature and horizontal velocity are smoothed vertically with two passes of the filter [1/4, 2/4, 1/4] before the local Ri is computed.

order to explain the diurnal cycle of deep turbulence dissipation. Moum and Caldwell (1985) considered nighttime convective overturns as a possible primary cause. They argued that such a mechanism is unlikely because dissipation in the 30–50 m range was larger than at the 10–30 m depth range. Our LES results in the absence of an EUC support this conclusion. In this case nocturnal convective cooling does cause a diurnal cycle of turbulence below the mixed layer, but the penetration is too shallow to account for the observed deep strong dissipation and the phase of its vertical propagation. Moum and Caldwell (1985) also considered the possibility that daytime solar turbulence suppression is responsible, but argued that the penetration of such daytime suppression to a depth of 90 m is unlikely. This hypothesis was later discounted by observations under light wind conditions (e.g., TH2; Peters et al. 1994).

Gregg et al. (1985) considered three possible mechanisms of the deep diurnal cycle turbulence. The first was the solar suppression hypothesis, similar to that of Moum and Caldwell (1985). The second was that the diurnal variation of shear and/or stratification, N^2, might be the cause, but they did not observe the expected diurnal cycles of shear and N^2 below the mixed layer. The third hypothesis was that downward propagating internal waves break in the stratified high-shear zone, producing much of the observed mixing. During the day, solar heating suppresses the source of internal waves, leading to a minimum mixing below the mixed layer. Using mooring data, McPhaden and Peters (1992) showed that energy spectrum exhibits a diurnal cycle at high wavenumbers. Moum et al. (1992) found strong correlation between internal wave activity and turbulence dissipation. These observations support the third hypothesis of Gregg et al. (1985).

By including an EUC, the LES model is able to reproduce the deep diurnal cycle of turbulence. It is found that turbulence exhibits a diurnal cycle within the mixed layer as well below the mixed layer. Turbulence exists as deep as more than twice the mixed layer depth. Although our model domain in experiment II is too small to resolve the internal waves of the observations, the turbulence dissipation from the model qualitatively agrees with many features of the observations. We have also found the fluid motions below the mixed layer to be very nonlinear, indicated by the order 1 ratio of fluctuating temperature gradient to mean temperature gradient. It is difficult to distinguish between linear internal waves in the presence of shear and turbulence.

We propose the following hypothesis. During the daytime intense solar heating, surface turbulence is directly suppressed due to the restratification and the associated increase of mean gradient Richardson number, which is a result of the asymmetry of surface forcing, namely, increased solar heating tends to increase the stratification rapidly while constant wind stress tends to maintain a constant shear near the surface even though the magnitude of velocity increases. The asymmetry of surface forcing causes a net increase in mean Ri, even though both shear and stratification increase after sunrise. The EUC shear region below the mixed layer is dynamically stable, with $0.25 <$ mean Ri < 0.50 and decaying turbulence the most common condition. Therefore, at depth during the day there is either no turbulence at all, or decaying turbulence. Near sunset, convection is initiated in the mixed layer and near-surface turbulence is enhanced. The mixed layer deepens due to the spreading of turbulence into the shear zone. The mean gradient Richardson number decreases due to the asymmetry of surface forcing; namely, convection tends to homogenize temperature while constant wind stress tends to maintain a constant shear near the surface. The net result is a decrease in mean Ri even though both shear and stratification decrease after sunset. If the mean Ri drops below 0.25, dynamic instability of the mean flow would occur, generating turbulence directly. At deeper depths and under relatively low mean Ri but stable condition, the following three processes contribute to the growing phase of the deep-cycle turbulence:

1) breaking of internal waves, generated by organized large eddies in the mixed layer, in the high-shear environment (Gregg et al. 1985);
2) local dynamic instability of the Kelvin–Helmholtz (K–H) type at local Ri not much below the critical value 0.25, caused by the perturbations of local shear and stratification by vertically propagating internal waves;
3) entrainment, which is more vigorous in the presence of shear and is directly linked to local K–H instability.

Shortly after sunrise, convection and internal wave production cease. Turbulence and internal wave activity below the mixed layer then decay. Thus, the daily cycle of turbulence below the mixed layer consists of growing and decaying phases.

The first two processes listed above can be nonlocal while the third process is local. The first process might not be easily detectable when the mean flow is near critical Richardson number Ri $= 0.25$. The waves might be so nonlinear that they become unstable right away, once generated, and transition to turbulence occurs rapidly (Fritts et al. 1996). We do not see systematic wave propagation and wave overturning from our LES solutions. So, the first process is not a major cause of the deep-cycle turbulence in the model. If mean Ri is already near the critical value of 0.25, dynamical instability can occur due to internal wave perturbation of the mean flow. We do see a diurnal cycle of distribution of local Ri, that is, more grid points with low local R_i at night than during the day. However, the motions below the mixed layer are highly nonlinear, that is, more turbulence-like than wavelike. So, the second process is not easily detectable from the model solutions. Once the boundary layer becomes fully turbulent, the processes 1) and 2) might be obscured by turbulent motions

and the entrainment process. The latter involves a wide range of length scales and the corrugated interface between turbulent fluid and nonturbulent fluid are determined by eddies of all sizes inside the boundary layer (Deardorff et al. 1969; Deardorff 1974). By entrainment, we also include the process of gradual spreading of turbulence from a turbulent region to a weakly turbulent region by direct contact. For example, after sunset, the decaying turbulence below the mixed layer becomes growing again through direct contact with the turbulent fluid above and through local K–H instability caused by turbulent or wave perturbations of the mean flow. The local K–H instability is the most important mechanism of generating the deep-cycle turbulence in our model.

The diurnal cycle of mean gradient Richardson number Ri is an integral part of the deep diurnal cycle of turbulence. The observations of Peters et al. (1988, 1991) and Lien et al. (1995) support this assertion. At 40 m, LES model shows that mean Ri varies from 0.25 to 0.4 (Fig. 12c), which is typical of the observations of Peters et al. (1988, see their Fig. 6). At 20 m, LES shows a larger range of mean Ri = [0.23, 0.9] for experiment II (Fig. 12b) while the observations of H. Peters (unpublished results, 1996 personal communication) show mean Ri varies typically from 0.02 to 0.3. However, experiment III (finest resolution of the three experiments) does show a smaller range of diurnal variation of mean (Ri = [0.1, 0.5] (figure not shown). This is consistent with the fact that turbulence dissipation from experiment III agrees better with the observations at shallow depths (dotted line in the top panel of Fig. 11).

Dillon et al. (1989) found that observationally derived vertical divergence of turbulent stress is too small to close the balance of the zonal momentum equation at the equator for the depth range 60–90 m, assuming typical conditions of the equatorial large-scale flow. Two of the possible reasons that they considered are 1) the production–dissipation balance method is flawed and 2) the dynamic role of internal waves might not be properly accounted for. From this LES study, we found that below the mixed layer, buoyant suppression ($\mathcal{B}$) can be significant, so neglecting this term tends to underestimate eddy viscosity by as much a factor of 2. If this correction is made, the imbalance will be reduced to 25% instead of the 70% in Dillion et al. (1989). However, Wijesekera and Dillon (1991) showed that wave momentum flux divergence due to westward propagating internal waves can be as large as turbulent stress divergence caused by wind. Lien et al. (1996) showed that momentum fluxes due to internal waves can be substantial based on observations, although it is not clear whether the momentum flux is completely due to internal waves or in part due to turbulence. From a two-dimensional study, Skyllingstad and Denbo (1994) also showed that internal waves generated by the interaction of diurnal forcing and equatorial undercurrent carry substantial momentum flux to depths well below the mixed layer even though three-dimensional turbulent motions are absent in their model.

Since our model does not resolve the observed internal waves (with typical wavelenghts of 150–300 m), we cannot adequately address the role of these internal waves in the dynamics of the deep-cycle turbulence. As one of the reviewers pointed out:

> . . . If we are to conclude that the model is capturing the essence of the problem, we must accept that the diurnal cycling of the energetic internal waves at these scales is a coincidental rather than fundamental aspect of the observations. I am not compelled by the model results to accept this, particularly in light of the lack of convergence of the results as the horizontal domain size is increased.

The reviewer is correct that we cannot rule out the possibility that these waves, which could be generated by large-scale organized convective eddies at nighttime, have a direct link to the generation of small-scale turbulence through K–H instability, and wave breaking based on the present study. A LES study with much larger horizontal domains to cover several wavelengths of the observed internal waves is needed to further address the role of internal waves in the dynamics of deep-cycle turbulence. We should also point out that such a study would also require a finer resolution than that used in the present study because even with a resolution of 2.5 m $\times$ 2.5 m $\times$ 1 m (expt III), the diurnal cycle of small-scale overturning is not resolved. Ideally, a sequence of numerical experiments with increasing domain sizes should be conducted to address the convergence issue. The LES experiments presented here are on the lower end of this sequence with relatively coarse horizontal resolution. Vertical resolution of less than 1 m might also be desirable to better resolve the wave overturning because wave breaking and transition to turbulence might occur at much smaller scales even though internal waves with relatively long wavelengths (150–300 m) provide the major source of energy.

It should be noted that there are substantial differences between the LES results and observations. For example, at 60 m, turbulence dissipation of the LES can be smaller than that of the TH1 (Peters et al. 1994) by about a factor of 2 or more (Fig. 11, bottom panel). Part of the differences might be explained by the difference in environmental conditions. But it is possible that part of the differences are indeed due to the lack of internal waves in our model. This is an open question and future studies are needed.

A major justification for measuring turbulence dissipation rates is to infer vertical mixing coefficients for both momentum (viscosity, K_m) and density (diffusivity, K_ρ). To do so requires assumptions regarding the TKE budget equation (13), where the ratio of buoyant suppression ($\mathcal{B} > 0$ in stably stratified turbulence) to shear production is the flux Richardson number, $R_f = \mathcal{B}/\mathcal{S}$. Under the assumption of a balance between shear pro-

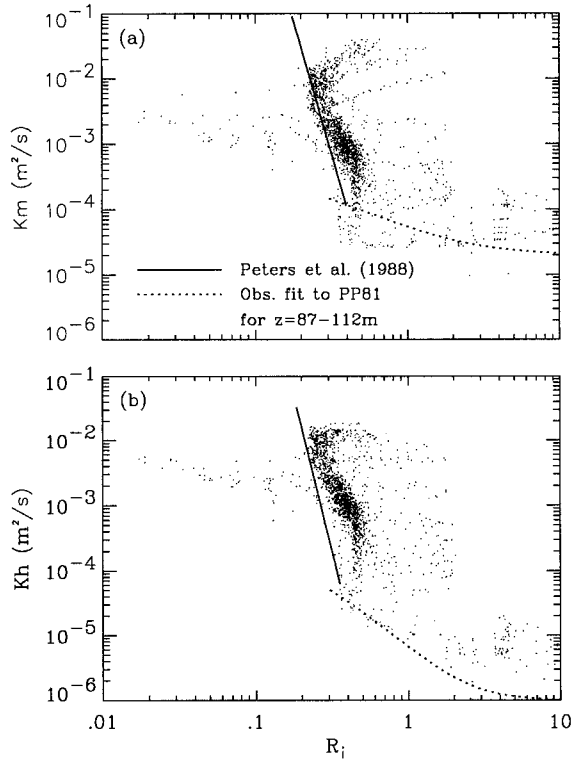

FIG. 16. (a) Eddy viscosity K_m and (b) diffusivity K_h as functions of mean gradient Richardson number for experiment II. The solid lines are taken from the fit to observations of Peters et al. (1988) for the depth range 23–81 m. The dotted lines are observational fit to the parameterization of Pacanowski and Philander (1981) for the depth range 87–112 m (Peters et al. 1988).

duction, buoyant suppression, and dissipation, the commonly used expressions are

$$K_m = \frac{\epsilon}{(1 - R_f)u_z^2}, \qquad K_\rho = \frac{R_f}{(1 - R_f)}\frac{\epsilon}{N^2}. \quad (15)$$

The latter is derived by Osborn (1980), who argues for $R_f \leq 0.15$. The former is given by Peters et al. (1988), who use the same argument to ignore R_f, as a small term. However, Fig. 9 indicates that this contention may not hold in the equatorial conditions of the LES experiments, which show that R_f varies typically between 0.2 and 0.5 for the depth range 30–80 m.

The turbulent eddy coefficients of K_m and $K_h = K_\rho$ have been computed from hourly averaged turbulence fluxes, velocity shear, and temperature gradient from the LES solutions. The results from experiment II, day 6 are shown in Fig. 16 along with the Peters et al. (1988) analytical fit to observations. The variation of K_m with the mean gradient Richardson number Ri has a similar shape as the case without EUC (case A2 of Wang et al. 1996, Fig. 7b). In both cases K_m agrees with the observationally derived values of Peters et al. (1988) near Ri = 0.25. Large values (in excess of 0.01 $m^2\ s^{-1}$) of K_m do occur at depths of about 10–20 m. These high values are due to nighttime convection and result from vigorous nonlocal mixing in the presence of small vertical gradients. There is an entrainment zone, which is in the depth range 60–80 m. This zone is characterized by mean Ri $\approx$ 1 for the case without an EUC (Wang et al. 1996) and by mean Ri $\approx$ 0.4–0.5 for the case with an EUC. As a result, the agreement between LES and observations is better for the case with an EUC. The eddy diffusivity coefficient has similar functional dependency on mean Ri as the observations of Peters et al. (1988).

In general, LES still predicts higher values of eddy viscosity and diffusivity than observational estimates. Part of this bias may be due to the underestimation of mixing coefficients from dissipation measurements. Figure 9 indicates that under the equatorial conditions of the LES experiments, the flux Richardson number is neither constant, nor always negligible. It is highly variable in time and space. There are regions with $R_f \approx 0.40$ over long periods of time (e.g., at 65-m depth between 0400 and 1000 and between 1600 and 2200, inferring from Fig. 9). Such high values, if not accounted for, would result in underestimates of both mixing coefficients. The variability implies that observational fits will depend on the space–time sampling of the measurements.

Fundamentally, eddy viscosity and diffusivity might not be simple functions of mean Ri alone. The dependence could be $K_m = f$ (Ri, u_z^2, N^2), for example. This functionality is justified if one considers the limit of mean Ri approaching zero, which gives $K_m = F(u_z^2)$, a function of shear only. There still might be some dependence on shear even in the case of finite mean Ri [compare the shape of K_m vs Ri relation in Fig. 7 of Wang et al. (1996) and Fig. 16]. This might also contribute to the discrepancies between the observations and the LES results because our environmental conditions are not identical to the conditions of the observations. Finally, the resolution of our LES model is relatively coarse, especially in the horizontal plane, and the sensitivity of LES solutions to subgrid-scale parameterizations is not fully explored. These modeling aspects need to be improved in the future.

Acknowledgments. We thank C.-H. Moeng and Peter Sullivan for providing the original LES code and for helpful discussions. We are very grateful to Peter Gent for his help in running the Gent–Cane model and for insightful discussions. Assistance from Brian Kaufman in running the Gent–Cane model is greatly appreciated. We thank Ren-Chieh Lien and Hartmut Peters for providing their observational data, for helpful comments, and sharing unpublished results. William D. Smyth made helpful suggestions and comments. Helpful comments by Eric Firing are greatly appreciated. Comments by the anonymous reviewers were helpful in clarifying some points and in improving the presentation of the manuscript. During this study, D. Wang was supported by a postdoctoral fellowship from the Advanced Study

Program, National Center for Atmospheric Research, which is sponsored by the National Science Foundation.

APPENDIX A

Parameterization of Subgrid-Scale Eddy Viscosity and Diffusivity

Subgrid-scale Reynolds stress tensor is defined by

$$\tau_{ij} = -\overline{u_i' u_j'} = \begin{cases} \kappa_{mh}(u_{i,j} + u_{j,i}), & i, j = 1, 2 \\ \kappa_{mv}(u_{i,j} + u_{j,i}), & i \text{ or } j = 3. \end{cases}$$

The subgrid turbulent heat flux is given by

$$q_i = -\overline{u_i' T'} = \begin{cases} \kappa_{hh} T_{,i}, & i = 1, 2 \\ \kappa_{hv} T_{,3}, & i = 3. \end{cases}$$

Turbulence dissipation is defined as

$$\epsilon = c_\epsilon \frac{e^{3/2}}{l_\epsilon},$$

where $\mathbf{u} = (u, v, w)$[2] is the velocity resolved by the LES model, τ is the unresolved subgrid Reynolds stress tensor, $\mathbf{q} = (q_1, q_2, q_3)$ is the subgrid heat flux vector, e is the subgrid turbulent kinetic energy, and ϵ is the turbulence dissipation. Note that the horizontal and the vertical diffusion coefficients are the same for the vertical velocity w. This is necessary for energetic consistency. Namely, the Reynolds stress tensor should not appear in the total (mean plus turbulent) kinetic energy equation.

Instead of using a single eddy viscosity and diffusivity coefficient (Wang et al. 1996), we adopt horizontal and vertical diffusion coefficients for both momentum and heat. The horizontal diffusion coefficients are

$$\kappa_{mh} = c_k \Delta \sqrt{e}, \qquad \kappa_{hh} = c_h \Delta \sqrt{e}, \tag{A1}$$

and the vertical diffusion coefficients are

$$\kappa_{mv} = c_k l \sqrt{e}, \qquad \kappa_{hv} = c_h l \sqrt{e}, \tag{A2}$$

where

$$c_k = 0.0856, \qquad c_h = 0.204, \qquad c_\epsilon = 0.845,$$

and $\Delta = (\Delta x \Delta y \Delta z)^{1/3}$. Here Δx, Δy, and Δz are model grid spacings in the zonal, meridional, and vertical directions.

The length scales l and l_ϵ are functions of shear and stratification, in general. Here we adopt the following rules of length scales (Cheng and Canuto 1994; Schumann 1991; Wang et al. 1996):

$$l_\epsilon = \Delta$$

$$l = \Delta \left(1 + c_l \frac{N^2 \Delta^2}{e} \mathcal{H}(N^2) \right)^{-1}, \qquad z < z_o \tag{A3}$$

$$l = \Delta \left[1 + 0.021 \frac{(\overline{u}_z^2 + \overline{v}_z^2)\Delta^2}{e} \mathcal{H}(N^2) \right]^{-3/2}, \qquad 0 > z \geq z_o, \tag{A4}$$

where $N^2 = \alpha g \overline{T}_z$, $c_l = 1.2$, and $z_o = -3$ m. However, when (A3) gives a smaller value of l near the surface, we use (A3) instead of (A4) for l. We also set a minimum value of $l = l_{\min} = 0.3\Delta$ allowed above the depth of z_o. If the primary balance near the surface in the subgrid-scale kinetic energy equation is between shear production (due to vertical shear of horizontal velocity) and dissipation, vertical eddy viscosity κ_{mv} can be written as

$$\kappa_{mv} = (C_s \Delta)^2 (\overline{u}_z^2 + \overline{v}_z^2)^{1/2},$$

where

$$C_s = \left(\frac{l^3}{\Delta^3} \frac{c_k^3}{c_\epsilon} \right)^{1/4}$$

is the Smagorinsky constant (Smagorinsky 1963; Lilly 1967). The minimum value of C_s is 0.067, when $l = l_{\min} = 0.3\Delta$. Deardorff (1970) used $C_s = 0.1$. Some investigators have used $C_s = 0.065$ (e.g., Moin and Kim 1982) for wall turbulence (also see Reynolds 1989 and references therein). Overbars represent horizontal mean.

We set minimum background vertical diffusion coefficients of

$$(\kappa_{mv})_{\min} = 2.5 \times 10^{-5} \text{ m}^2 \text{ s}^{-1}$$

and

$$(\kappa_{hv})_{\min} = 5.0 \times 10^{-6} \text{ m}^2 \text{ s}^{-1},$$

for numerical reasons, as in Wang et al. (1996). We also set minimum horizontal diffusion coefficients of

$$(\kappa_{mh})_{\min} = 1.0 \times 10^{-4} \text{ m}^2 \text{ s}^{-1}$$

and

$$(\kappa_{hh})_{\min} = 2.0 \times 10^{-5} \text{ m}^2 \text{ s}^{-1}.$$

The eddy viscosity tensor $\mathbf{K}$ in (4) is defined as

$$\mathbf{K} = \begin{pmatrix} \kappa_{mh} & 0 & 0 \\ 0 & \kappa_{mh} & 0 \\ 0 & 0 & \kappa_{mv} \end{pmatrix}.$$

APPENDIX B

Artificial Horizontal Diffusion at the Core of Equatorial Undercurrent

There is a technical difficulty of conducting spinup LES experiments with the presence of equatorial un-

[2] We will use (u, v, w) and (u_1, u_2, u_3) interchangeably for writing convenience.

dercurrent. At the core of the EUC, velocity is at its maximum while turbulence is at its minimum level because of the lack of shear. Therefore, the subgrid-scale turbulent kinetic energy equation (4) along with (A1) and (A2) predicts minimum values of viscosity and diffusivity. Actually these values are smaller than the minimum background diffusion coefficients chosen. This gives rise to huge grid Peclet and Reynolds numbers. For example, for an EUC core speed of 0.8 m s^{-1}, the background viscosity and diffusity coefficients chosen (appendix A), and zonal grid size of 5 m, the grid Peclet and Reynolds numbers are Pe = 200 000 and Re = 40 000. It is impossible to carry out a long integration with these large grid Peclet and Reynolds numbers without encountering numerical problems. This is true regardless of whether we include the large-scale equatorial flows or not. We therefore employ artificial horizontal diffusion of momentum and heat in the depth range of 80–150 m to avoid numerical instabilities. The momentum and heat equations, respectively, acquired the following terms:

$$A_m(z)\nabla_h^2\mathbf{u} \quad \text{and} \quad A_m(z)\nabla_h^2 T,$$

where ∇_h is the horizontal gradient operator; $A_m(z)$ linearly increases from zero at 80 m to 1.736×10^{-3} m^2 s^{-1} at 100 m and remains constant in the depth range 100–130 m, and then linearly decreases to zero at 150 m. The maximum value of artificial diffusion coefficient, which occurs well below the boundary layer, corresponds to a grid diffusive timescale of 4 h for a horizontal resolution of 5 m. This timescale is much larger than the typical timescale of motions in the entrainment zone (on the order of 1 min). We found that the horizontal scales of motions below the turbulent boundary layer tend to be large (on the order of several hundred meters) and therefore are not resolved by our model grid. So, this artificial diffusion has little effect on damping the motions below the boundary layer besides making the integration stable.

The added artificial diffusion also translates into an artificial dissipation in the horizontally averaged turbulent kinetic energy equation

$$A_m(z)(\overline{u_x''^2} + \overline{u_y''^2} + \overline{v_x''^2} + \overline{v_y''^2} + \overline{w_x''^2} + \overline{w_y''^2}),$$

where double primes denote resolved velocity fluctuations (residue from instant horizontal averages) and the overbars represent horizontal averages. We found this artificial dissipation to be rather small, on the order of 1.0×10^{-9} m^2 s^{-3} at most.

That the boundary layer depth is about 80 m after 6 days of integration is incidental, not related to the depth of artificial diffusion, which is 80 m. If we integrate the model much longer so that the boundary layer further deepens below 80 m, the depth below which artificial diffusion is applied should be further increased in order not to interfere with the turbulent processes within the boundary layer. We should point out that it is the sharp increase of gradient Richardson number below the boundary layer that limits the deepening of the boundary layer.

APPENDIX C

Equation for Horizontally Averaged Total Turbulent Kinetic Energy

Horizontally averaged total turbulent kinetic energy (resolved plus subgrid-scale) is governed by

$$\begin{aligned}\overline{E}_t + \overline{e}_t = &-[(\overline{\overline{u'w'}} + \overline{u''w''})\overline{u}_z + (\overline{\overline{v'w'}} + \overline{v''w''})\overline{v}_z] \\ &- [(\overline{Ew''} + \overline{ew''})_z + (\overline{\overline{u'w'}\,u''} + \overline{\overline{v'w'}\,v''} + \overline{\overline{w'w'}\,w''})_z] \\ &-[\overline{pw''} - 2(\overline{k_{mv}e})_z]_z + \alpha g[\overline{\overline{w'T'}} + \overline{w''T''}] - \overline{\epsilon} \\ &- [\overline{u''u''}\,U_x + \overline{u''v''}\,U_y + \overline{u''v''}\,V_x + \overline{v''v''}\,V_y + \overline{u''w''}\,W_x + \overline{v''w''}\,W_y + W\overline{E}_z],\end{aligned}$$

where e is the subgrid-scale turbulent kinetic energy and E is the resolved turbulent kinetic energy defined as

$$E = \frac{1}{2}(u''u'' + v''v'' + w''w'').$$

Double primes represent fluctuations (deviation from horizontal average). Single primes represent subgrid-scale quantities, and overbars represent horizontal average (the overbar in $\overline{u'w'}$ means average on the subgrid level, not horizontal average of the LES domain). The first term on the right-hand side (the two terms inside the square brackets) is shear production ($\mathcal{S}$), the second term (five terms inside the square brackets) is turbulent transport (T), the third term is work done by the fluctuating pressure ($\mathcal{P}$), the fourth term is buoyant suppression/production ($\mathcal{B}$), and the fifth term is turbulence dissipation ($\overline{\epsilon}$), of the turbulent kinetic energy. The last term (the last line) is advection of TKE due to large-scale advection, which is very small compared to other terms under the scale-separation hypothesis described in section 2. For example, the advection term ($W\overline{E}_z$) is much smaller than turbulent transport term T because the large-scale upwelling velocity W is several orders

of magnitude smaller than the turbulent fluctuation of vertical velocity w.

Note that turbulent transport (T) involves the correlations between the subgrid-scale stresses and the resolved eddy field (e.g., $\overline{u'w'u''}$). If subgrid-scale eddy viscosity coefficient κ_{mv} is only a function of z or constant (with laminar flow being a special case), these correlations simply reduce to the vertical diffusion of the resolved turbulent kinetic energy: $\kappa_{mv}\,\overline{E}_{zz}$. If there is a wide scale separation between the subgrid and resolved motions, these correlations should be small. Unfortunately this is not always the case for LES. We found the correlations between subgrid stresses and resolved velocity field to be comparable to $\overline{Ew''}$ within the mixed layer and small below the mixed layer. However, the total transport term is rather small in the TKE budget in the present study.

REFERENCES

Bryden, H. I., and E. C. Brady, 1989: Eddy momentum and heat fluxes and their effects on the circulation of the equatorial Pacific ocean. *J. Mar. Res.*, **47,** 55–79.

Cheng, Y., and V. M. Canuto, 1994: Stably stratified shear turbulence: A new model for the energy dissipation length scale. *J. Atmos. Sci.,* **51,** 2384–2396.

Chereskin, T. K., J. N. Moum, P. J. Stabeno, D. R. Caldwell, C. A. Paulson, L. A. Regier, and D. Halpern, 1986: Fine-scale variability at 140°W in the equatorial Pacific. *J. Geophys. Res.,* **91,** 12 887–12 897.

Deardorff, J. W., 1970: A numerical study of three-dimensional turbulent channel flow at large Reynolds numbers. *J. Fluid Mech.,* **41,** 453–480.

——, 1974: Three-dimensional numerical study of turbulence in an entraining mixed layer. *Bound.-Layer Meteor.,* **7,** 199–226.

——, G. E. Willis, and D. K. Lilly, 1969: Laboratory studies of nonsteady penetrative convection. *J. Fluid Mech.,* **35,** 7–31.

Dillon, T. M., J. N. Moum, T. K. Chereskin, and D. R. Caldwell, 1989: Zonal momentum balance at the equator. *J. Phys. Oceanogr.,* **19,** 561–570.

Fritts, D. C, J. F. Garten, and O. Andreassen, 1996: Wave breaking and transition to turbulence in stratified shear flows. *J. Atmos. Sci.,* **53,** 1057–1085

Gent, P. R., and M. A. Cane, 1989: A reduced gravity, primitive equation model of the upper equatorial ocean. *J. Comput. Phys.,* **81,** 444–480.

Gregg, M. C., H. Peters, J. C. Wesson, N. S. Oakey, and T. J. Shay, 1985: Intensive measurements of turbulence and shear in the equatorial undercurrent. *Nature,* **318,** 140–144.

Jerlov, N. G., 1968: *Optical Oceanography.* Elsevier, 194 pp.

Klemp, J. B., and D. R. Durran, 1983: An upper boundary condition permitting internal gravity wave radiation in numerical mesoscale models. *Mon. Wea. Rev.,* **111,** 430–444.

Large, W. G., J. C. McWilliams, and S. Doney, 1994. Oceanic vertical mixing: A review and a model with a nonlocal boundary layer parameterization. *Rev. Geophys.,* **32,** 363–403.

Lien, R.-C., D. R. Caldwell, M. C. Gregg and J. N. Moum, 1995: Turbulence variability at the equator in the central Pacific at the beginning of the 1991–1993 El Niño. *J. Geophys. Res.,* **100,** 6881–6898.

——, D. J. McPhaden, and M. C. Gregg, 1996: High-frequency internal waves at 0°, 140°W and their possible relationship to deep-cycle turbulence. *J. Phys. Oceanogr.,* **26,** 581–600.

Lilly, D. K., 1967: The representation of small scale turbulence in numerical simulation experiments. *Proc. IBM Sci. Comput. Symp. on Environmental Science,* Thomas J. Watson Research Center, Yorktown Heights, NY, 195–210.

McDougall, T. J., 1984: The relative roles of diapycnal and isopycnal mixing on subsurface water mass conversion. *J. Phys. Oceanogr.,* **14,** 1577–1589.

McPhaden, M. J., and H. Peters, 1992: Diurnal cycle of internal wave variation in the equatorial Pacific Ocean: Results from moored observations. *J. Phys. Oceanogr.,* **22,** 1317–1329.

Moeng, C. H., 1984: A large-eddy-simulation model for the study of planetary boundary-layer turbulence. *J. Atmos. Sci.,* **41,** 2052–2062.

Moin, P., and J. Kim, 1982. Numerical investigation of turbulent channel flow. *J. Fluid Mech.,* **118,** 341–377.

Moum, J. N., and D. R. Caldwell, 1985: Local influences on the shear-flow turbulence in the equatorial ocean. *Science,* **230,** 315–316.

——, ——, and C. A. Paulson, 1989: Mixing in the equatorial surface layer and thermocline. *J. Geophys. Res.,* **94,** 2005–2021.

——, D. Hebert, C. A. Paulson, and D. R. Caldwell, 1992: Turbulence and internal waves at the equator. Part I: statistics from towed thermistors and a microstructure profiler. *J. Phys. Oceanogr.,* **22,** 1330–1345.

Osborn, T. R., 1980: Estimates of the local rate of vertical diffusion from dissipation measurements. *J. Phys. Oceanogr.,* **10,** 83–89.

Pacanowski, R. C., and S. G. H. Philander, 1981: Parametrization of vertical mixing in numerical models of tropical oceans. *J. Phys. Oceanogr.,* **11,** 1443–1451.

Paulson, C. A., and J. J. Simpson, 1977: Irradiance measurements in the upper ocean. *J. Phys. Oceanogr.,* **7,** 952–956.

Peters, H., M. C. Gregg, and J. M. Toole, 1988: On the parameterization of equatorial turbulence. *J. Geophys. Res.,* **93,** 1199–1218.

——, ——, and T. B. Sanford, 1991: Equatorial and off-equatorial fine-scale and large-scale shear variability at 140°W. *J. Geophys. Res.,* **96,** 16 913–16 928.

——, ——, and ——, 1994: The diurnal cycle of upper equatorial ocean: Turbulence, fine-scale shear, and mean shear. *J. Geophys. Res.,* **99,** 7707–7723.

Price, J. F., R. A. Weller, and R. Pinkel, 1986: Diurnal cycling: Observations and models of the upper ocean responses to diurnal heating, cooling, and wind mixing. *J. Geophys. Res.,* **91,** 8411–8427.

Reynolds, W. C., 1989: The potential and limitations of direct and large eddy simulations. *Wither Turbulence? Turbulence at the Crossroads,* J. L. Lumley Ed., Lecture Notes on Physics, Vol. 357, Springer-Verlag, 313–343.

Schudlich, R. R., and J. F. Price, 1992: Diurnal cycles of current, temperature, and turbulent dissipation in a model of the equatorial upper ocean. *J. Geophys. Res.,* **97,** 5409–5422.

Schumann, U., 1991: Subgrid length-scales for large-eddy simulation of stratified turbulence. *Theor. Comput. Fluid Dyn.,* **2,** 279–290.

Skyllingstad, E. D., and D. W. Denbo, 1994: The role of internal gravity waves in the equatorial current system. *J. Phys. Oceanogr.,* **24,** 2093–2110.

Smagorinsky, J., 1963: General circulation experiment with the primitive equations. I. The basic experiment. *Mon. Wea. Rev.,* **91,** 99–164.

Sullivan, P. P., J. C. McWilliams, and C.-H. Moeng, 1996: A grid nesting method for large-eddy simulation of planetary boundary-layer flows. *Bound.-Layer Meteor.,* **80,** 167–202.

Wang, D., W. G. Large, and J. C. McWilliams, 1996. Large-eddy simulation of the equatorial ocean boundary layer: Diurnal cycling, eddy viscosity, and horizontal rotation. *J. Geophys. Res.,* **101,** 3649–3662.

Wijesekera, H. W., and T. M. Dillon, 1991: Internal waves and mixing in the upper equatorial Pacific Ocean. *J. Geophys. Res.,* **96,** 7115–7126.